https://www.science.org/doi/10.1126/science.abq3616; SCIENCE 8 Sep 2022 Vol 377, Issue 6613 pp. 1406-1412

Controlling the nucleation and growth kinetics of lead halide perovskite quantum dots

Quinten A. Akkerman,[1,2†] Tan P. T. Nguyen,[3] Simon C. Boehme,[1,2] Federico Montanarella,[1,2‡] Dmitry N. Dirin,[1,2] Philipp Wechsler,[1] Finn Beiglböck,[2] Gabriele Rainò,[1,2] Rolf Erni,[4] Claudine Katan,[3] Jacky Even[5] and Maksym V. Kovalenko[1,2*]

[1]Department of Chemistry and Applied Biosciences, ETH Zürich, Zürich CH-8093, Switzerland

[2]Empa-Swiss Federal Laboratories for Materials Science and Technology, Dübendorf, CH-8600, Switzerland

[3]Univ Rennes, ENSCR, INSA Rennes, CNRS, ISCR - UMR 6226, F-35000 Rennes, France

[4]Electron Microscopy Center, Empa – Swiss Federal Laboratories for Materials Science and Technology, Dübendorf, Switzerland.

[5]Univ Rennes, INSA Rennes, CNRS, Institut FOTON - UMR 6082, F-35000 Rennes, France

Current address:

[†]Lehrstuhl für Photonik und Optoelektronik, Nano-Institut München und Fakultät für Physik, Ludwig-Maximilians-Universität (LMU), Königinstr. 10, D-80539 München, Germany

[‡]Seaborough BV, Matrix VII Innovation Center, Science Park 106, 1098 XG Amsterdam, The Netherlands

*Corresponding author. mvkovalenko@ethz.ch

https://www.science.org/doi/10.1126/science.abq3616; SCIENCE 8 Sep 2022 Vol 377, Issue 6613 pp. 1406-1412

Abstract:
Colloidal lead halide perovskite (LHP) nanocrystals are of interest as photoluminescent quantum dots (QDs) whose properties depend on the size and shape. They are normally synthesized on subsecond time scales through hard-to-control ionic metathesis reactions. We report a room-temperature synthesis of monodisperse, isolable spheroidal $APbBr_3$ QDs (A=Cs, formamidinium, methylammonium) that are size-tunable from 3 to over 13 nanometers. The kinetics of both nucleation and growth are temporally separated and drastically slowed down by the intricate equilibrium between the precursor ($PbBr_2$) and the $A[PbBr_3]$ solute, with the latter serving as a monomer. QDs of all these compositions exhibit up to four excitonic transitions in their linear absorption spectra, and we demonstrate that the size-dependent confinement energy for all transitions is independent of the A-site cation.

One-Sentence Summary: Highly monodisperse lead-halide perovskite nanocrystals are synthesized via slow and temporally separated nucleation and growth, governed by the monomer supply rate.

https://www.science.org/doi/10.1126/science.abq3616; SCIENCE 8 Sep 2022 Vol 377, Issue 6613 pp. 1406-1412

Colloidal LHP nanocrystals (NCs) are light-emissive materials (*1, 2*) of practical interest for light-emitting diodes (LEDs) (*3, 4*), liquid crystal displays (LCDs) (*5*), lasers (*6*), scintillators (*7, 8*) and luminescent solar concentrators (*9, 10*). These materials exhibit several favorable photoluminescent (PL) properties, including near-unity PL quantum yields (QYs), a PL peak tailorable across the 410 to 800 nm spectral range, small PL full-width at half-maximum (FWHM, <100 meV), large absorption cross sections, long exciton coherence times, and fast (subnanosecond) radiative rates at low temperatures (*11-13*). Of rising scientific interest are single-photon emission from LHP NCs (*13-17*) and collective phenomena in LHP NC assemblies such as superfluorescence (*18-21*).

Given their synthetic availability, most studies on colloidal LHP NCs focused on relatively large NC sizes with diameters of around or exceeding 10 nm. In this weak excitonic confinement regime, tunability of the bandgap energy is predominantly achieved through mixed-halide compositions. Being structurally soft with mainly ionic chemical bonding, LHP NCs differ rather orthogonally from more conventional QD materials such as CdSe and InP that have covalent bonding and rigid crystal structures. This difference manifests in the difficulty in producing small LHP QDs (only a few nanometers in diameter) and has hindered the studies into the strong size-quantization of excitons in LHPs (and possible practical use) as well as understanding of the mechanism of LHP QD formation.

The high lattice ionicity and low lattice formation energy of LHP NCs lead to challenges for the synthesis of small QDs. They form too quickly during ionic co-precipitation, with subsecond formation kinetics. In this regard, the surface capping ligands, which are crucially important for the controlled nucleation and growth as well as for the structural integrity of the resulting QDs and their stability against solvents and environment, bind in a noncovalent and dynamic manner (*22*), which also adds to the difficulty of arresting QD formation and stabilizing them at small sizes.

Monodispersity and shape-uniformity, as well as precise size-tunability in the sub-10 nm regime requires a scalable synthesis that yields isolable, pure and robust QD samples. Limited success had been reached for $CsPbX_3$ (X Cl, Br, and I) compositions (*21, 23, 24*), wherein QD fractions down to 3 to 4 nm were obtained postsynthetically. However, the synthesis yield was small for a specific QD size fraction, mainly because of the initial broad size dispersion or very lossy isolation. Long-chain zwitterionic capping ligands exhibited improved surface adhesion relative to more conventional single-binding-head molecules and rendered the small $CsPbBr_3$ QDs sufficiently robust to sustain multiple steps of size-selective precipitation leading to monodisperse fractions (*21*). Small colloidal $FAPbX_3$ and $MAPbX_3$ NCs (where FA is formamidinium and MA is methylammonium) remained elusive as they are even more labile structurally.

We reasoned that the slower formation of small monodisperse LHP QDs at full reaction yield cannot be accomplished by only mere adjustments of typical reaction parameters, such as lowering of the reaction temperature and concentration of reagents. We hypothesized that precursor-monomer-QD nuclei conversion path must be characterized by the mutual chemical equilibrium between these moieties governed by the common complexing agent, thus having a self-limiting character. Importantly, this equilibrium should not be obscured by any competing process, such as binding of a stronger capping ligand to the QD surface or constituting ions. The latter condition somewhat goes against the previous efforts on stabilizing the perovskite NC surfaces by stronger binding ligands.

We found that trioctylphosphine oxide (TOPO) served this three-fold requirement as it complexes (solubilizes) the $PbBr_2$ precursor, binds to the $Cs[PbBr_3]$ monomer (solute), and then weakly coordinates to the QD nuclei surface. The issue of isolation and subsequent robustness of the obtained QDs was then mitigated by adding a stronger binding ligand – lecithin as a long-chain

https://www.science.org/doi/10.1126/science.abq3616; SCIENCE 8 Sep 2022 Vol 377, Issue 6613 pp. 1406-1412

zwitterion – at the end of the QD formation step (not during their synthesis). We thus present a room-temperature synthesis, in which the overall QD formation occurred on a time scale of up to 30 min, which also allowed the in-situ observation of the reaction by optical absorption and emission spectroscopy. After isolation, monodisperse rhombicuboctahedral $CsPbBr_3$ QDs, with mean size tunable between 3 and 13 nm range, were obtained at 100% precursor-to-QD conversion rate. These $CsPbBr_3$ QDs, as well as $FAPbBr_3$ and $MAPbBr_3$ QDs obtained analogously, exhibited up to four well-resolved excitonic transitions, and the size-dependent confinement energies for all transitions was independent of the A-site cations. The obtained energies of these transitions, utilizing the statistics from over 25.000 individual spectra, agreed with those calculated using effective mass/**k·p** model. We anticipate that analogous "low ionic strength" reactions will be developed for precision synthesis of NCs of other structurally soft metal halides as well as for engineering complex metal halide NC heterostructures.

Synthesis of monodisperse $CsPbBr_3$ QDs

We hypothesized that conventional approaches, which we refer to as oleylamine - oleic acid (OLAM/OA) path (*25*), suffers from the rapid conversion of the $PbBr_2$ into high concentrations of haloplumbate ionic solute ($PbBr_3^-$) upon the action of OLAM/OA (*26, 27*). The subsequent reaction with injected Cs-ions was thus quantitative and fast, and hence nucleation and growth were not temporally separated. We aimed at establishing the mechanism, in which the formation of $PbBr_3^-$ anions was activated by the introduction of Cs-cations, by having the latter as the only available cation in the system throughout the synthesis. The equilibrium was retained with the non-reactive $PbBr_2$ precursor reservoir through a common coordinating agent, in this case the neutral molecule trioctylphosphine oxide (TOPO) as a sole coordinating agent for solubilizing $PbBr_2$ precursor (**Fig. 1, A and B**) (*28*). We injected cesium-diisooctylphosphinate (Cs-DOPA) solution into this $PbBr_2$:TOPO solution at room temperature (both in hexane; see **Materials and Methods**, **Supplementary Text and figs. S1 to S5)**. Both TOPO and DOPA are weakly binding ligands for LHP QDs (*28, 29*) and hence were readily displaced with lecithin, a strongly binding zwitterionic ligand (*30*), for subsequent isolation and purification steps as well as ex-situ characterization (see detailed comparison of in-situ and ex-situ data analysis, as well as the in-situ set up in **figs. S6 to S13**). The reaction volume can be readily scaled to yield gram-scale quantities of QDs with identical optical properties (**Table S3** and **fig. S14**). The stability of the obtained QDs of all sizes for at least one year is seen as a retention of identical absorption spectra (**fig**. **S15**).

In-situ optical absorption spectra (**Fig. 1C and Movie S1,** 6 nm $CsPbBr_3$ QDs) recorded the slow growth over 30 min that led to a narrow size dispersion, as evidenced by sharp excitonic absorption peaks. Purified lecithin-coated QDs exhibited the same sharp absorption features when measured ex-situ and could be prepared from 3 to 13 nm in diameter (**Fig. 1D and S16**), with an average PLQY of 87 ± 3 % for QD size down to 4 nm, and 72 ± 7% for 3 to 4 nm QDs. In-situ synchrotron SAXS (Small-Angle X-ray Scattering) measurements (6.2 nm QDs, **Fig. 1E**) revealed a narrow size dispersion (8.1%) and rather isotropic spheroidal particle shapes. The latter was in stark contrast to previous ex-situ SAXS measurements on cuboidal shaped $CsPbBr_3$ QDs, where on average a 20% offset between the shortest and longest edge length of the cuboid was reported (*21, 30*). The findings also held for 12 nm-large QDs (**fig. S17**).

TEM (Transmission Electron Microscopy) and scanning TEM (STEM) images of purified 8 nm QDs (**Fig. 1F and S18)** revealed a preference for hexagonal packing, indicating spheroidal QDs, rather than the commonly observed nanocubes (*20, 21, 23, 25*). High-resolution STEM (HR-STEM) of 12 nm QDs showed truncation along the {110} and {111} facets, hence rhombicuboctahedral shape of QDs (**fig. S19**), in good-agreement with the spheroidal shape in in-

https://www.science.org/doi/10.1126/science.abq3616; SCIENCE 8 Sep 2022 Vol 377, Issue 6613 pp. 1406-1412

situ SAXS. $CsPbBr_3$ QDs crystallize in a phase-pure orthorhombic phase as seen from in-situ WAXS (Wide-Angle X-ray Scattering) of crude solutions as well as powder x-ray diffraction (XRD, **Fig. 1G**). $CsPb(Cl:Br)_3$ QDs, which exhibit larger bandgaps compared to $CsPbBr_3$, and are of interest for blue LEDs, could be obtained with this method by applying an in-situ anion exchange, using $ZnCl_2$-TOPO solution added before lecithin ligand (**fig. S20**).

In-situ optical measurements allowed for thorough and fast parametric screening. The overall dilution and the concentration of the TOPO ligands were most effective for controlling the QD size in our room-temperature synthesis, contrary to conventional size control by varying the reaction temperature (*21, 23, 25, 30*). For example, dilution of the reaction by an order of magnitude led to a decrease in size from 9 to 3 nm (**Fig. 1, H and I, and fig. S21**). Similar size changes resulted by adjusting the concentrations of $PbBr_2$ or Cs-DOPA precursors individually (**figs. S1 to S4**). Alternatively, a fourfold increase in TOPO concentration increased the QD size from ~ 3 to 9 nm (**Fig. 1, J and K**). A combined effect of dilution and larger TOPO concentration translated into drastically slower QD growth (**Fig. 1L, fig. S22, and Movie S2**).

Spheroidal versus cuboidal QDs

Thus far, reported colloidal perovskite NCs were mostly of {001}-bound, cuboidal shape (*25*), which can be ascribed to commonly used alklyammonium ligands stabilizing the planes of fully built PbX_6-octahedra (AX as terminating surface planes) with ammonium moieties incorporated by substituting the surface A-cations. The absence of cationic and other strongly binding surfactants in the present study may explain the tendency to form spheroidal NCs, exposing several crystal facets. We elucidated the origin of the exceptionally well-resolved excitonic transitions in the spheroidal QDs. The difference could not be attributed merely to the size dispersion. For example, **Fig. 2, A and B,** compare our spheroidal $CsPbBr_3$ QDs with several of our own examples of cuboidal $CsPbBr_3$ QDs with same or better size dispersion (**fig. S23**). The latter include NCs capped with didodecyldimethylammonium bromide (DDAB) or OLAM/OA, as used recently for NC superlattices (*20*), as well as those capped with long-chain sulfobetaine zwitterionic ligands (3-(*N*,*N*-dimethyloctadecylammonio)propanesulfonate, or ASC18) after size-selective precipitation (*21*, *31*). The similarity of PL FWHM across these different shapes also evidences that the inhomogeneous broadening was not the cause for the "blurred" higher order absorption transitions in cuboidal QDs either.

We analyzed the effect of the shape itself by computing a one-photon absorption cross-section (**Fig. 2, C and D, and fig. S24**). For this, the effective mass approximation (EMA) was used with an energy-dependent effective mass to emulate the effect of full two-band coupling (*32*). The electron-hole Coulomb interaction was included in a single-shot calculation (that is, without self-consistency iteration, see details in **Supporting Text).** Compared to a perfect sphere, the cubic symmetry introduced a perturbation that coupled the spherical states of different angular momenta. This coupling led to mixing between and splitting of the higher order absorption states, which resulted in the experimentally observed smoothing out of the absorption spectra. Furthermore, recent SAXS studies on cuboidal $CsPbBr_3$ NCs revealed up to 20% reduction in length along one of the cuboid edges (oblation), which further contributed to the splitting of higher order absorption states (*21, 30*). In particular, the transition from a spherical shape to an oblate cuboidal shape led to the nearly complete flatting of the second and third absorption transitions.

Reaction mechanism

https://www.science.org/doi/10.1126/science.abq3616; SCIENCE 8 Sep 2022 Vol 377, Issue 6613 pp. 1406-1412

We used in-situ optical absorption spectra to understand how the use of a solely neutral coordinating agent (TOPO) prevents premature and uncontrolled conversion of $PbBr_2$ into the $PbBr_3^-$ solute. $PbBr_2$ dissolved in TOPO to form a $PbBr_2$[TOPO] complex (*28*) that had a broad absorption peak around 4.4 eV (**Fig. 3A**). Its intensity change allowed us to monitor the depletion of $PbBr_2$ during the reaction. Only upon the injection of Cs-DOPA did $PbBr_3^-$ appear in the course of 100 ms, as evidenced as an additional peak emerging at lower energies (3.85 eV) (**fig. S25**), from the formation of a $PbBr_3^-$ complex (*27, 33*). Once the accumulation of $PbBr_3^-$ surpassed a nucleation threshold (supersaturation), $CsPbBr_3$ QDs formed (on the order of seconds, **Fig. 3B**). More conventional ligands for $CsPbBr_3$ QDs, such as OA or OLAM, reacted with the $PbBr_2$[TOPO] complex (*28*), but free DOPA on its own did not (**fig. S26)**.

As the only counter-ion available to $PbBr_3^-$ is Cs^+, we assumed the formation of a Cs[$PbBr_3$] complex (tight ionic pair) as the concentration of $PbBr_3^-$ species scaled with Cs-DOPA concentration (**fig. S27A**). A Cs[$PbBr_3$] complex might be additionally coordinated by TOPO. Importantly, a higher TOPO concentration suppressed the formation of Cs[$PbBr_3$], indicating that it formed in equilibrium (**fig. S27B)** with the more stable $PbBr_2$[TOPO] species. Particularly, an injection of additional TOPO after the initial Cs-DOPA injection decomposed the Cs[$PbBr_3$] complex back into $PbBr_2$ species **(fig. S28)**.

An overall precursor-to-QDs path is depicted in **Fig. 3C**. We illustrate the effect of TOPO-driven $PbBr_2$:Cs[$PbBr_3$] equilibrium on the formation of $CsPbBr_3$ QDs for a stoichiometric $PbBr_2$:Cs-DOPA = 3:2 reaction by plotting in-situ monitored $PbBr_2$, Cs[$PbBr_3$] and $CsPbBr_3$ concentrations (**Fig. 3D).** An immediate decrease of $PbBr_2$ concentration upon injection of Cs-DOPA was accompanied by the formation of Cs[$PbBr_3$]. As the reaction progressed, Cs[$PbBr_3$] complexes were converted into $CsPbBr_3$ QDs nuclei, and both $PbBr_2$ and Cs[$PbBr_3$] species were proportionally consumed but remained present, consistent with the $PbBr_2$:Cs[$PbBr_3$] equilibrium. The stoichiometric conversion $3PbBr_2 \rightarrow 2PbBr_3^- + Pb^{2+}$ was confirmed by subtracting Cs[$PbBr_3$] and $CsPbBr_3$ concentrations to yield the $PbDOPA_2$ concentration. The reaction eventually reached near 100% yield **(fig. S29)**.

The rate-limiting step in this reaction was the conversion of the Cs[$PbBr_3$] intermediate into $CsPbBr_3$. A reaction with a fourfold excess of $PbBr_2$ compared to Cs-DOPA (**fig. S30**) showed that the Cs[$PbBr_3$] complex solely acted as an intermediate for the $CsPbBr_3$ QDs and was not stable on its own. The $PbBr_2$:Cs[$PbBr_3$] equilibrium self-limited the available amount Cs[$PbBr_3$] for both the nucleation, as well as the subsequent growth of $CsPbBr_3$ QDs. The separation of nucleation and growth, a prerequisite for the narrow size dispersion, was evident from a comparison of the QD concentration versus the $CsPbBr_3$ molar concentration evolution (**Fig. 3e and Movie S3**). The self-limiting equilibrium mechanism also explained the larger QD size and lower reaction rate with increasing TOPO concentration, which shifted the equilibrium toward $PbBr_2$, reducing the available quantity of Cs[$PbBr_3$] for the nucleation and hence decreasing the number of nuclei (and the final QD concentration, **Fig. 3F),** while the overall yield remained relatively unchanged **(fig. S31)**. For example, a fourfold increase in TOPO concentration increased the particle size from 3.5 to 8.7 nm, corresponding to a 14-fold increase in QD volume. The QD concentration correspondingly dropped 15 times. Additional experiments confirming the self-limiting equilibrium mechanism are described in the **Supporting Text**. We also note that other approaches to finely controlled in-situ generation of monomers, for instance by molecular engineering of the library of precursors, have been successful for metal chalcogenide NCs (*34*).

Optical properties of $CsPbBr_3$ QDs

https://www.science.org/doi/10.1126/science.abq3616; SCIENCE 8 Sep 2022 Vol 377, Issue 6613 pp. 1406-1412

Higher-order excitonic transitions, along with their size- and shape-dependencies, have been assigned in CdSe and PbS QDs (*35, 36*), but the corresponding datasets for $CsPbBr_3$ QDs have been very limited, and typically only the lowest two transitions (1s-1s and 1p-1p) are reported (*21, 37*). We were able to resolve the first four excitonic transitions readily resolved both in-situ (see **Fig. 4A and Movie S4** for various final QD sizes) and ex-situ linear absorption spectra (**Fig. 4B**). Size dependencies captured by 25,000 in-situ experimental spectra recorded for 2.5 to 11 nm QDs (see **Fig. 4C** for examples) were retained in the purified QDs (**Fig. 4D**).

To assign the absorption features, the specific excitonic transitions were calculated with a two-band $\boldsymbol{k.p}$ model (*21, 37*). The Coulomb interaction was included under the self-consistent Hartree-Fock approximation. For the 1s-1s, 1p-1p, 1d-1d, and 1f-1f transitions, we found good agreement of the theoretical and experimental transition energies, plotted relative to the first excited state (1s-1s) as a function of their first excited state energies (**Fig. 4F**) (*35*). The spheroidal $CsPbBr_3$ QDs optically behaved as confined model systems with symmetrical electron and hole manifolds, which had approximately equal effective masses. The theoretical absorption spectrum was then obtained from calculations of the oscillator strength for all allowed transitions using second-order many-body perturbation theory, which allowed for partial incorporation of correlation effects in the electron-photon interaction (*32, 38*). Each transition was broadened with a normalized Voigt line-shape, and the results for all transitions were added to obtain the final absorption spectra shown, for instance, for 7.0 nm (**Fig. 4G and S32).**

This model was further extended for a broad range of temperatures between 14 and 300 K, as shown in **fig. S33**. More discussion on the broadening mechanisms is found in the **Supporting Text** and **fig. S34**. The calculated low-temperature absorption spectrum was compared to the PL excitation (PLE) spectrum at 14 K (**Fig. 4H**). Whereas only one 1p-1p state transition was expected and observed at room-temperature, the narrowing of the absorption features upon cooling to 14 K revealed two 1p-1p contributions, separated by ~70 meV. This splitting was observed in temperature-dependent absorption spectra for various QD sizes (**fig S35**) and was previously ascribed to the shape-asymmetry in cuboidal QDs (oblation in one direction) (*21, 37*).

A likewise observation in isotropic spheroidal QDs called for other considerations, such as anisotropies of the effective mass of electrons or holes that arose from the orthorhombic crystal structure of the $CsPbBr_3$ (*39, 40*). Such anisotropic effects were already inferred from electrical characteristics (*41*). Inclusion of 10 to 15% of anisotropy in the electron hole mass gave rise to the splitting of the 1p-1p transition with the magnitude found experimentally **(figs. S36 to S38**). The splitting of the 1p states potentially had a fairly complex dependence on the QD size and temperature; see further discussion in **the Supporting Text**.

Simultaneous in-situ acquisition of both absorption and PL spectra allowed us to study the inherent size-dependent Stokes shift (**fig. S39 and Movies S1 and S5)** with excellent energy accuracy (standard deviation of only about 2% in the range of 4 to 10 nm**, fig. S40**). The measured Stokes shift agreed with recent calculations that assume an intrinsic confined hole state with size-dependent alignment above the valence band maximum (*42*).

Extension to $FAPbBr_3$ and $MAPbBr_3$ QDs

We extended the synthesis methodology to hybrid small organic-inorganic LHP QDs (**Fig. 5**). $FAPbBr_3$ QDs were synthesized by replacing Cs_2CO_3 with FA-acetate and DOPA with a mixture of DOPA and OA. $FAPbBr_3$ QDs were observed to form an order of magnitude faster compared to $CsPbBr_3$ QDs (minutes time scale, see **Fig. 5A** for in-situ absorption in the synthesis of 7 nm $FAPbBr_3$ QDs). Analogous experiments with MA-acetate gave rise to a size-series of

https://www.science.org/doi/10.1126/science.abq3616; SCIENCE 8 Sep 2022 Vol 377, Issue 6613 pp. 1406-1412

monodisperse $MAPbBr_3$ NCs, albeit with further reduction of the synthesis time to ~ 10 s **(Fig. 5E).** Such a pronounced effect of the A-site cation on the reaction rate agreed with the proposed reaction mechanism (**Fig. 3C**), wherein coordination of A-cation to $PbBr_3^-$ was hypothesized to govern the stability and hence reactivity of these transient species. Size series of 6 to 11 nm lecithin-capped $FAPbBr_3$ and $MAPbBr_3$ QDs (**Fig. 5B and 5F**), which were found to be quasispherical in shape (**Fig. 5, C and G**), were analogous to $CsPbBr_3$ QDs. These hybrid LHP NCs had narrow size dispersion of under 10% and well-resolved excitonic peaks in both in-situ and ex-situ measurements (see **Fig 5D, 5H and S41**). Notably, the faster formation kinetics did not jeopardize the utility of the synthesis, as the QD size control is accomplished at a full reaction yield by adjusting the concentrations, not the growth time. We compared all three LHP homologs as they featured an analogous Pb-halide octahedral framework. As illustrated in **Fig. 5I,** the 7-nm $CsPbBr_3$, $FAPbBr_3$, and $MAPbBr_3$ QDs exhibited nearly identical absorption spectra, when matching the positions of their first excitonic transition. Moreover, across the experimental and theoretical size series, all three materials exhibited the same effect of quantum confinement on higher-order excitonic transitions (**Fig. 5J and fig. S42**). High room-temperature PL QY (80-100%) along with sharp and tunable excitonic features, and facile processing into diverse photonic structures, make small LHP QDs an attractive emitter of choice for studying strong light-matter interaction, such as exciton-polariton condensates and polaritonic lasing.

References and Notes

1. Q. A. Akkerman, G. Rainò, M. V. Kovalenko, L. Manna, Genesis, challenges and opportunities for colloidal lead halide perovskite nanocrystals. *Nat. Mater.* **17**, 394-405 (2018).
2. A. Dey *et al.*, State of the Art and Prospects for Halide Perovskite Nanocrystals. *ACS Nano* **15**, 10775-10981 (2021).
3. Y.-H. Kim *et al.*, Comprehensive defect suppression in perovskite nanocrystals for high-efficiency light-emitting diodes. *Nat. Photonics* **15**, 148-155 (2021).
4. Y. Hassan *et al.*, Ligand-engineered bandgap stability in mixed-halide perovskite LEDs. *Nature* **591**, 72-77 (2021).
5. www.avantama.com.
6. Q. Zhang, Q. Shang, R. Su, T. T. H. Do, Q. Xiong, Halide Perovskite Semiconductor Lasers: Materials, Cavity Design, and Low Threshold. *Nano Lett.* **21**, 1903-1914 (2021).
7. Q. Chen *et al.*, All-inorganic perovskite nanocrystal scintillators. *Nature* **561**, 88-93 (2018).
8. M. Gandini *et al.*, Efficient, fast and reabsorption-free perovskite nanocrystal-based sensitized plastic scintillators. *Nat. Nanotechnol.* **15**, 462-468 (2020).
9. M. Wei *et al.*, Ultrafast narrowband exciton routing within layered perovskite nanoplatelets enables low-loss luminescent solar concentrators. *Nat. Energy* **4**, 197-205 (2019).
10. J. Wu *et al.*, Efficient and Stable Thin-Film Luminescent Solar Concentrators Enabled by Near-Infrared Emission Perovskite Nanocrystals. *Angew. Chem. Int.* **59**, 7738-7742 (2020).
11. M. A. Becker *et al.*, Long Exciton Dephasing Time and Coherent Phonon Coupling in $CsPbBr_2Cl$ Perovskite Nanocrystals. *Nano Lett.* **18**, 7546-7551 (2018).
12. G. Rainò *et al.*, Single Cesium Lead Halide Perovskite Nanocrystals at Low Temperature: Fast Single-Photon Emission, Reduced Blinking, and Exciton Fine Structure. *ACS Nano* **10**, 2485-2490 (2016).

https://www.science.org/doi/10.1126/science.abq3616; SCIENCE 8 Sep 2022 Vol 377, Issue 6613 pp. 1406-1412

13. H. Utzat *et al.*, Coherent single-photon emission from colloidal lead halide perovskite quantum dots. *Science* **363**, eaau7392 (2019).
14. P. Tamarat *et al.*, The ground exciton state of formamidinium lead bromide perovskite nanocrystals is a singlet dark state. *Nat. Mater.* **18**, 717-724 (2019).
15. Y.-S. Park, S. Guo, N. S. Makarov, V. I. Klimov, Room Temperature Single-Photon Emission from Individual Perovskite Quantum Dots. *ACS Nano* **9**, 10386-10393 (2015).
16. C. Yin *et al.*, Bright-Exciton Fine-Structure Splittings in Single Perovskite Nanocrystals. *Phys. Rev. Lett.* **119**, 026401 (2017).
17. K. Cho *et al.*, Luminescence Fine Structures in Single Lead Halide Perovskite Nanocrystals: Size Dependence of the Exciton–Phonon Coupling. *Nano Lett.* **21**, 7206-7212 (2021).
18. G. Rainò *et al.*, Superfluorescence from lead halide perovskite quantum dot superlattices. *Nature* **563**, 671-675 (2018).
19. F. Mattiotti, M. Kuno, F. Borgonovi, B. Jankó, G. L. Celardo, Thermal Decoherence of Superradiance in Lead Halide Perovskite Nanocrystal Superlattices. *Nano Lett.* **20**, 7382-7388 (2020).
20. I. Cherniukh *et al.*, Perovskite-type superlattices from lead halide perovskite nanocubes. *Nature* **593**, 535-542 (2021).
21. F. Krieg *et al.*, Monodisperse Long-Chain Sulfobetaine-Capped $CsPbBr_3$ Nanocrystals and Their Superfluorescent Assemblies. *ACS Cent. Sci.* **7**, 135-144 (2021).
22. J. De Roo *et al.*, Highly Dynamic Ligand Binding and Light Absorption Coefficient of Cesium Lead Bromide Perovskite Nanocrystals. *ACS Nano* **10**, 2071-2081 (2016).
23. Y. Dong *et al.*, Precise Control of Quantum Confinement in Cesium Lead Halide Perovskite Quantum Dots via Thermodynamic Equilibrium. *Nano Lett.* **18**, 3716-3722 (2018).
24. M. Imran *et al.*, Shape-Pure, Nearly Monodispersed $CsPbBr_3$ Nanocubes Prepared Using Secondary Aliphatic Amines. *Nano Lett.* **18**, 7822-7831 (2018).
25. L. Protesescu *et al.*, Nanocrystals of Cesium Lead Halide Perovskites ($CsPbX_3$, X = Cl, Br, and I): Novel Optoelectronic Materials Showing Bright Emission with Wide Color Gamut. *Nano Lett.* **15**, 3692-3696 (2015).
26. G. Almeida *et al.*, Role of Acid–Base Equilibria in the Size, Shape, and Phase Control of Cesium Lead Bromide Nanocrystals. *ACS Nano* **12**, 1704-1711 (2018).
27. J. Hui *et al.*, Unveiling the Two-Step Formation Pathway of Cs_4PbBr_6 Nanocrystals. *Chem. Mater.* **32**, 4574-4583 (2020).
28. G. Almeida *et al.*, The Phosphine Oxide Route toward Lead Halide Perovskite Nanocrystals. *J. Am. Chem. Soc.* **140**, 14878-14886 (2018).
29. Y. Shynkarenko *et al.*, Direct Synthesis of Quaternary Alkylammonium-Capped Perovskite Nanocrystals for Efficient Blue and Green Light-Emitting Diodes. *ACS Energy Lett.* **4**, 2703-2711 (2019).
30. F. Krieg *et al.*, Stable Ultraconcentrated and Ultradilute Colloids of $CsPbX_3$ (X = Cl, Br) Nanocrystals Using Natural Lecithin as a Capping Ligand. *J. Am. Chem. Soc.* **141**, 19839-19849 (2019).
31. F. Krieg *et al.*, Colloidal $CsPbX_3$ (X = Cl, Br, I) Nanocrystals 2.0: Zwitterionic Capping Ligands for Improved Durability and Stability. *ACS Energy Lett.* **3**, 641-646 (2018).
32. P. C. Sercel, J. L. Lyons, N. Bernstein, A. L. Efros, Quasicubic model for metal halide perovskite nanocrystals. *J. Chem. Phys.* **151**, 234106 (2019).

https://www.science.org/doi/10.1126/science.abq3616; SCIENCE 8 Sep 2022 Vol 377, Issue 6613 pp. 1406-1412

33. S. J. Yoon, K. G. Stamplecoskie, P. V. Kamat, How Lead Halide Complex Chemistry Dictates the Composition of Mixed Halide Perovskites. *J. Phys. Chem. Lett.* **7**, 1368-1373 (2016).
34. M. P. Hendricks, M. P. Campos, G. T. Cleveland, I. Jen-La Plante, J. S. Owen, A tunable library of substituted thiourea precursors to metal sulfide nanocrystals. *Science* **348**, 1226-1230 (2015).
35. D. J. Norris, M. G. Bawendi, Measurement and assignment of the size-dependent optical spectrum in CdSe quantum dots. *Phys. Rev. B* **53**, 16338-16346 (1996).
36. A. D. Andreev, A. A. Lipovskii, Anisotropy-induced optical transitions in PbSe and PbS spherical quantum dots. *Phys. Rev. B* **59**, 15402-15404 (1999).
37. W. Shcherbakov-Wu, P. C. Sercel, F. Krieg, M. V. Kovalenko, W. A. Tisdale, Temperature-Independent Dielectric Constant in $CsPbBr_3$ Nanocrystals Revealed by Linear Absorption Spectroscopy. *J. Phys. Chem. Lett.* **12**, 8088-8095 (2021).
38. T. P. T. Nguyen, S. A. Blundell, C. Guet, One-photon absorption by inorganic perovskite nanocrystals: A theoretical study. *Phys. Rev. B* **101**, 195414 (2020).
39. T. Sakuma *et al.*, Low-energy excitation in $CsPbX_3$ (X=Cl, Br). *Solid State Ion.* **154-155**, 237-242 (2002).
40. B. Traoré *et al.*, Efficient and accurate calculation of band gaps of halide perovskites with the Tran-Blaha modified Becke-Johnson potential. *Phys. Rev. B* **99**, 035139 (2019).
41. P. Zhang *et al.*, Anisotropic Optoelectronic Properties of Melt-Grown Bulk $CsPbBr_3$ Single Crystal. *J. Phys. Chem. Lett.* **9**, 5040-5046 (2018).
42. M. C. Brennan *et al.*, Origin of the Size-Dependent Stokes Shift in $CsPbBr_3$ Perovskite Nanocrystals. *J. Am. Chem. Soc.* **139**, 12201-12208 (2017).

Supporting references

43. L. Chao *et al.*, Room-Temperature Molten Salt for Facile Fabrication of Efficient and Stable Perovskite Solar Cells in Ambient Air. *Chem* **5**, 995-1006 (2019).
44. J. Maes *et al.*, Light Absorption Coefficient of $CsPbBr_3$ Perovskite Nanocrystals. *J. Phys. Chem. Lett.* **9**, 3093-3097 (2018).
45. A. Guinier, G. Fournet, Small-Angle Scattering of X-Rays. *John Wiley & Sons* (1951).
46. M. Burian, H. Amenitsch, Dummy-atom modelling of stacked and helical nanostructures from solution scattering data. *IUCrJ* **5**, 390-401 (2018).
47. L. Jones *et al.*, Smart Align—a new tool for robust non-rigid registration of scanning microscope data. *Adv. Struct. Chem. Imaging.* **1**, 8 (2015).
48. Q. A. Akkerman *et al.*, Nearly Monodisperse Insulator Cs_4PbX_6 (X = Cl, Br, I) Nanocrystals, Their Mixed Halide Compositions, and Their Transformation into $CsPbX_3$ Nanocrystals. *Nano Lett.* **17**, 1924-1930 (2017).
49. T. P. T. Nguyen, S. A. Blundell, C. Guet, Calculation of the biexciton shift in nanocrystals of inorganic perovskites. *Phys. Rev. B* **101**, 125424 (2020).
50. Z. Yang *et al.*, Impact of the Halide Cage on the Electronic Properties of Fully Inorganic Cesium Lead Halide Perovskites. *ACS Energy Lett.* **2**, 1621-1627 (2017).
51. K. Galkowski *et al.*, Determination of the exciton binding energy and effective masses for methylammonium and formamidinium lead tri-halide perovskite semiconductors. *Energy Environ. Sci.* **9**, 962-970 (2016).
52. J. J. Olivero, R. L. Longbothum, Empirical fits to the Voigt line width: A brief review. *J. Quant. Spectrosc. Radiat. Transfer* **17**, 233-236 (1977).

https://www.science.org/doi/10.1126/science.abq3616; SCIENCE 8 Sep 2022 Vol 377, Issue 6613 pp. 1406-1412

53. J. Ramade *et al.*, Exciton-phonon coupling in a $CsPbBr_3$ single nanocrystal. *Appl. Phys. Lett.* **112**, 072104 (2018).
54. M. Puppin *et al.*, Evidence of Large Polarons in Photoemission Band Mapping of the Perovskite Semiconductor $CsPbBr_3$. *Phys. Rev. Lett.* **124**, 206402 (2020).
55. C. C. Stoumpos *et al.*, Crystal Growth of the Perovskite Semiconductor $CsPbBr_3$: A New Material for High-Energy Radiation Detection. *Cryst. Growth Des.* **13**, 2722-2727 (2013).
56. C. A. López *et al.*, Crystal Structure Features of $CsPbBr_3$ Perovskite Prepared by Mechanochemical Synthesis. *ACS omega* **5**, 5931-5938 (2020).
57. M. Zhang *et al.*, Growth and characterization of all-inorganic lead halide perovskite semiconductor $CsPbBr_3$ single crystals. *CrystEngComm* **19**, 6797-6803 (2017).
58. P. Cottingham, R. L. Brutchey, Depressed Phase Transitions and Thermally Persistent Local Distortions in $CsPbBr_3$ Quantum Dots. *Chem. Mater.* **30**, 6711-6716 (2018).
59. M. C. Brennan, M. Kuno, S. Rouvimov, Crystal Structure of Individual $CsPbBr_3$ Perovskite Nanocubes. *Inorg. Chem.* **58**, 1555-1560 (2019).
60. Z.-L. Yu *et al.*, Oriented tuning the photovoltaic properties of γ-$RbGeX_3$ by strain-induced electron effective mass mutation. *J. Phys. D: Appl. Phys.* **50**, 465101 (2017).
61. C. Zhu *et al.*, Strain engineering in perovskite solar cells and its impacts on carrier dynamics. *Nat. Commun.* **10**, 815 (2019).
62. H.-S. Kim, N.-G. Park, Importance of tailoring lattice strain in halide perovskite crystals. *NPG Asia Mater.* **12**, 78 (2020).
63. K. Shibata, J. Yan, Y. Hazama, S. Chen, H. Akiyama, Exciton Localization and Enhancement of the Exciton–LO Phonon Interaction in a $CsPbBr_3$ Single Crystal. *J. Phys. Chem. C* **124**, 18257-18263 (2020).
64. X. Wang, Q. Wang, Z. Chai, W. Wu, The thermal stability of $FAPbBr_3$ nanocrystals from temperature-dependent photoluminescence and first-principles calculations. *RSC Adv.* **10**, 44373-44381 (2020).

Acknowledgments: We thank M. Blankenburg and U. Lienert for assistance during the SAXS and WAXS measurements. We thank F. Krumeich and I. Cherniukh for HAADF-STEM measurements and F. Krieg and I. Cherniukh for providing reference cuboidal $CsPbBr_3$ NCs. **Funding:** This work was financially supported by the European Union's through Horizon 2020 Research and innovation Programme through European Research Commission (ERC-CoG, agreement number 819740, project SCALE-HALO) and FET Open research and innovation action (grant agreement no. 899141, project PoLLoC), and by the Air Force Office of Scientific Research and the Office of Naval Research under award number FA8655-21-1-7013. SAXS and WAXS measurements were carried out at beamline P21.2 at PETRA III at DESY, a member of the Helmholtz Association (HGF); The research leading to this result has been supported by the project CALIPSOplus under the Grant Agreement 730872 from the EU Framework Programme for Research and Innovation HORIZON 2020. **Author contributions:** Q.A.A. performed the synthesis and optical characterization, with the contributions from P.W., F.B and D.N.D. T.P.T.N, C.K. and J.E. carried out theoretical calculations. S.C.B performed the low-temperature PLE measurements. F.M. carried out the WAXS and SAXS experiments. R.E. conducted electron microscopy. Q.A.A and M.V.K. wrote the manuscript, with input from all authors. M.V.K, G.R., C.K., and J.E. supervised the project. **Competing interests:** The authors

https://www.science.org/doi/10.1126/science.abq3616; SCIENCE 8 Sep 2022 Vol 377, Issue 6613 pp. 1406-1412

declare no competing interests. **Data and materials availability:** All data are available in the manuscript or the supplementary material.

Supplementary Materials

Materials and Methods
Supplementary Text
Figs. S1 to S42
Tables S1 and S2
References (*43-64*)
Movies S1 to S5

Fig. 1. Room-temperature, controlled-rate synthesis of monodisperse $CsPbBr_3$ QDs. A, A reaction scheme and overview of in-situ monitoring techniques. **B,** Overview of used ex-situ techniques on ligand exchanged and washed QDs which are complementary with the used in-situ techniques. **C,** Example of in-situ recorded absorption spectra of 6 nm QDs during 30 min reaction with solid line being the final recorded absorption spectrum, demonstrating clear and sharp first and higher order absorption peaks. **D,** Absorption spectra of series of washed $CsPbBr_3$ QDs ranging from roughly 3 to 13 nm. **E,** SAXS scattering curve of 6 nm QDs recorded at the end of a reaction, resulting in a size dispersion of roughly 8%, and a fitted pseudo spherical shape with one axis being slightly shorter compared to the other two. **F,** STEM image of washed 7.8 nm QDs and HRSTEM image of a single QD showing the pseudospherical shape arising from truncation. **G,** Diffractograms of 6.2 nm QDs recorded both in-situ in a crude solution using WAXS as well as from a washed dispersion using XRD on a film, both exhibiting a match with the orthorhombic crystal structure of $CsPbBr_3$. **H,** in-situ recorded size of $CsPbBr_3$ QDs at various concentrations (concentration of Cs-DOPA) showing both the decrease in size and reaction speed upon dilution. **I,** Respective final absorption spectra of reactions shown in panel H, indicating that all final samples are highly monodisperse. **J,** in-situ recorded size of $CsPbBr_3$ QDs at various $PbBr_2$:TOPO ratios (with a fixed $PbBr_2$ concentration) showing the increase in size with increasing TOPO concentration, while the reaction rate remained relatively unchanged. **K,** Respective final absorption spectra of reactions shown in panel C, indicating that all final samples are highly monodisperse. **L,** Comparison of reaction rates of three different reactions resulting in roughly the same QDs size, showing how controlling both the overall dilution and the TOPO concentration can slow down the reaction by two orders of magnitude.

Fig. 2. The effect of QD shape on the absorption spectral features. A and B, Experimental absorption and PL spectra of 5 nm and 9 nm cuboidal and spheroidal QDs. Monodisperse cuboidal QDs coated with DDAB (*20*), OLAM/OA (*20*), ACS18 (*21*). **C and D,** Calculated absorption spectra of both 5 and 9 nm QDs with different shapes using the effective mass approximation (EMA) with the inclusion of electron-hole Coulomb interaction in a single-shot calculation. For the cuboidal QD, an oblate shape was chosen with 20% shortening along one of the cube's edge (parameter b = 1.2).

Fig. 3. In-situ observation of the precursors-to-$CsPbBr_3$ QDs conversion. A, $PbBr_2$-TOPO solution before and within 5 s after the injection of Cs-DOPA. **B and C,** Typical evolution of the absorption spectra from $PbBr_2$ through $Cs[PbBr_3]$ monomer and $CsPbBr_3$ QDs and the

https://www.science.org/doi/10.1126/science.abq3616; SCIENCE 8 Sep 2022 Vol 377, Issue 6613 pp. 1406-1412

corresponding reaction path. **D,** Temporal evolution of precursors' and reaction products' concentrations for a stochiometric reaction (2:3 Cs-DOPA:$PbBr_2$), wherein both the $PbBr_2$ precursor and the $Cs[PbBr]_3$ intermediate are consumed upon the formation of $CsPbBr_3$ QDs. $PbBr_2$ and $Cs[PbBr]_3$ exist in equilibrium, as both are present until $PbBr_2$ is consumed. **E,** Effective separation of nucleation and growth, as well as absence of QD coalescence or Ostwald ripening is apparent from the QD concentration evolution and the respective reaction yield. **F,** QD concentration vs. time dependence at different TOPO concentrations. Higher TOPO quantities suppress the available $Cs[PbBr_3]$ monomer and hence the number of nuclei.

Fig. 4. Excitonic transitions in $CsPbBr_3$ QDs seen with in- and ex-situ spectroscopy corroborated with theoretical calculations. A, Typical second derivative of the absorption during the growth of $CsPbBr_3$ QDs, featuring up to four transitions that can be extracted using a peak finding algorithm. **B,** Second derivative absorption spectra for purified QDs. **C,** A compilation of the extracted in-situ transition energy values across several syntheses (n ~ 25000 individual absorption spectra). **D,** Similar data set obtained ex-situ from 15 different QD sizes. **E**, Energy level diagram used for the two-band ***k.p*** theory with Hartree-Fock level description of the Coulomb interaction (*32, 38*). **F,** Comparison of experimental relative absorption transitions and theoretical calculated states. **G**, Theoretical absorption spectrum in which the electron-photon interaction is considered within the framework of second-order many-body perturbation theory with the corresponding peak assignment. **H**, 14 K PLE spectrum revealing splitting of the 1p-1p transition caused by slight anisotropy in effective masses.

Fig. 5. Monodisperse $FAPbBr_3$ and $MAPbBr_3$ QDs and comparison with $CsPbBr_3$ QDs. A and E In-situ spectra during the formation of 7-nm QDs. **B and F** Absorption spectra of isolated series. **C and G,** STEM images of *ca*. 7 nm QDs. **D and H** In-situ, ex-situ and calculated excitonic transition energies plotted with respect to their first excitonic transition energy. **I,** Absorption spectra of ca. 7-nm $CsPbBr_3$, $FAPbBr_3$, and $MAPbBr_3$ QDs with matched 1s-1s transition energy. **J,** Experimental size-dependent relative peak position of $CsPbBr_3$, $FAPbBr_3$, and $MAPbBr_3$ QDs.

https://www.science.org/doi/10.1126/science.abq3616; SCIENCE 8 Sep 2022 Vol 377, Issue 6613 pp. 1406-1412

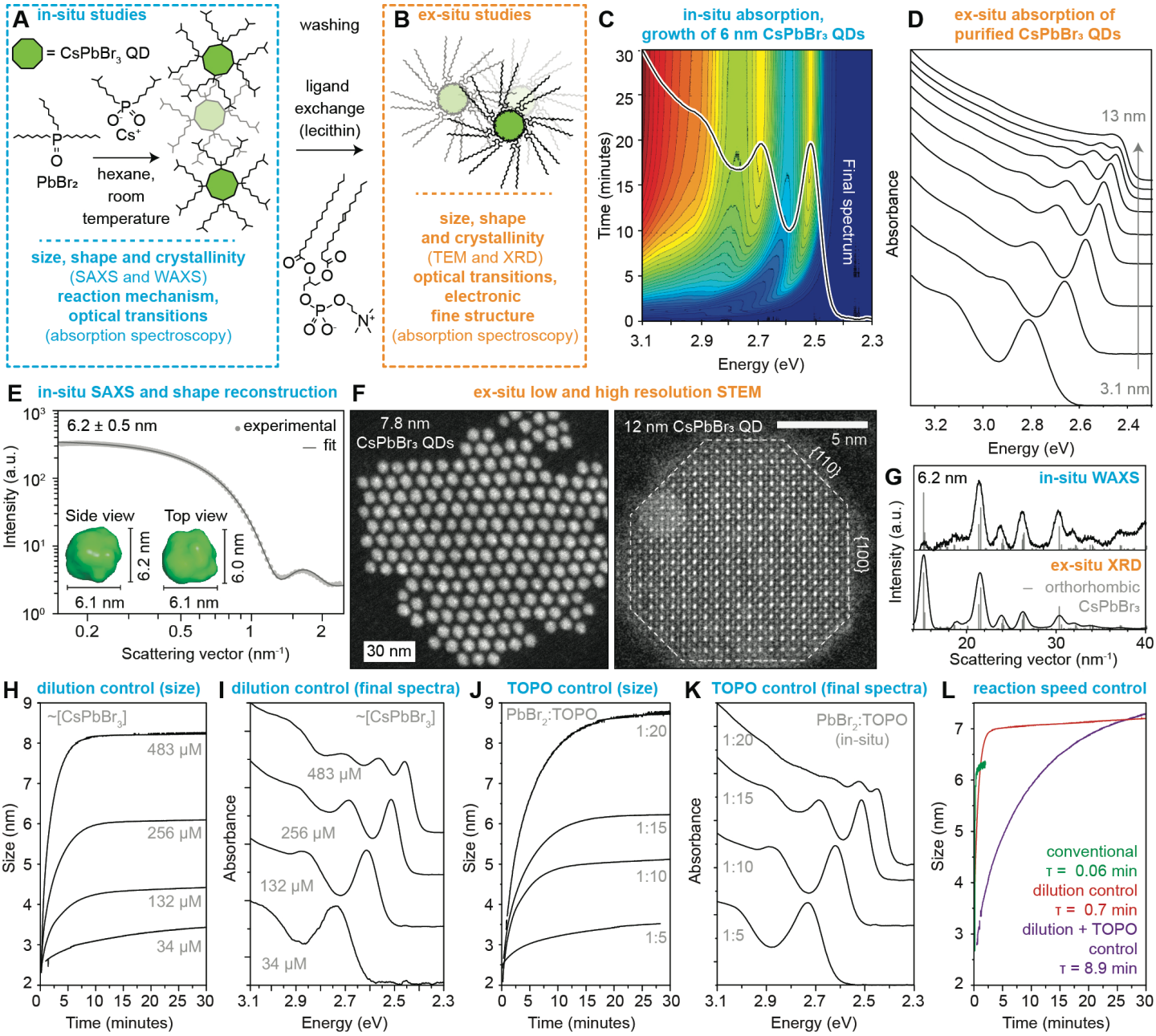

https://www.science.org/doi/10.1126/science.abq3616; SCIENCE 8 Sep 2022 Vol 377, Issue 6613 pp. 1406-1412

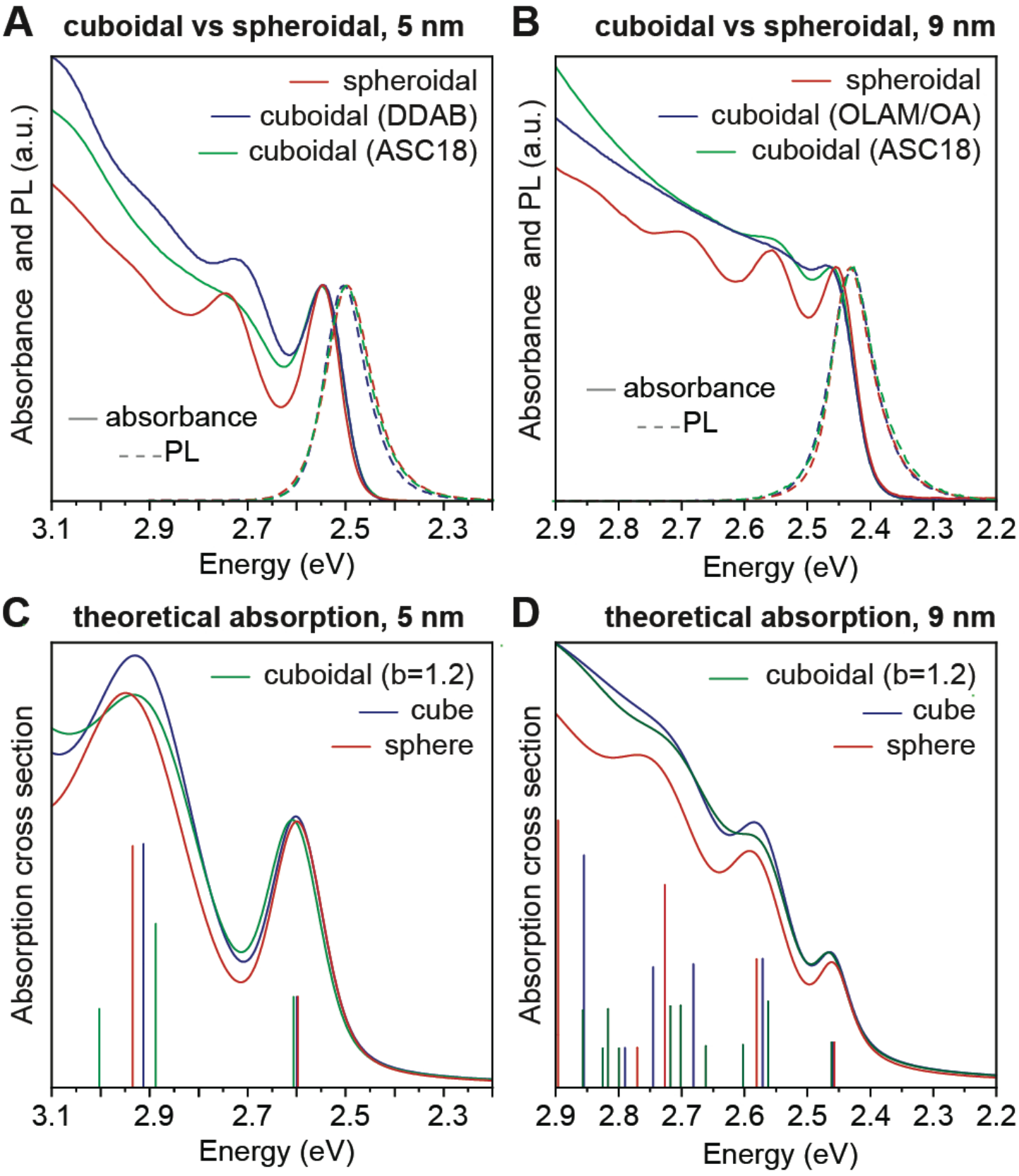

https://www.science.org/doi/10.1126/science.abq3616; SCIENCE 8 Sep 2022 Vol 377, Issue 6613 pp. 1406-1412

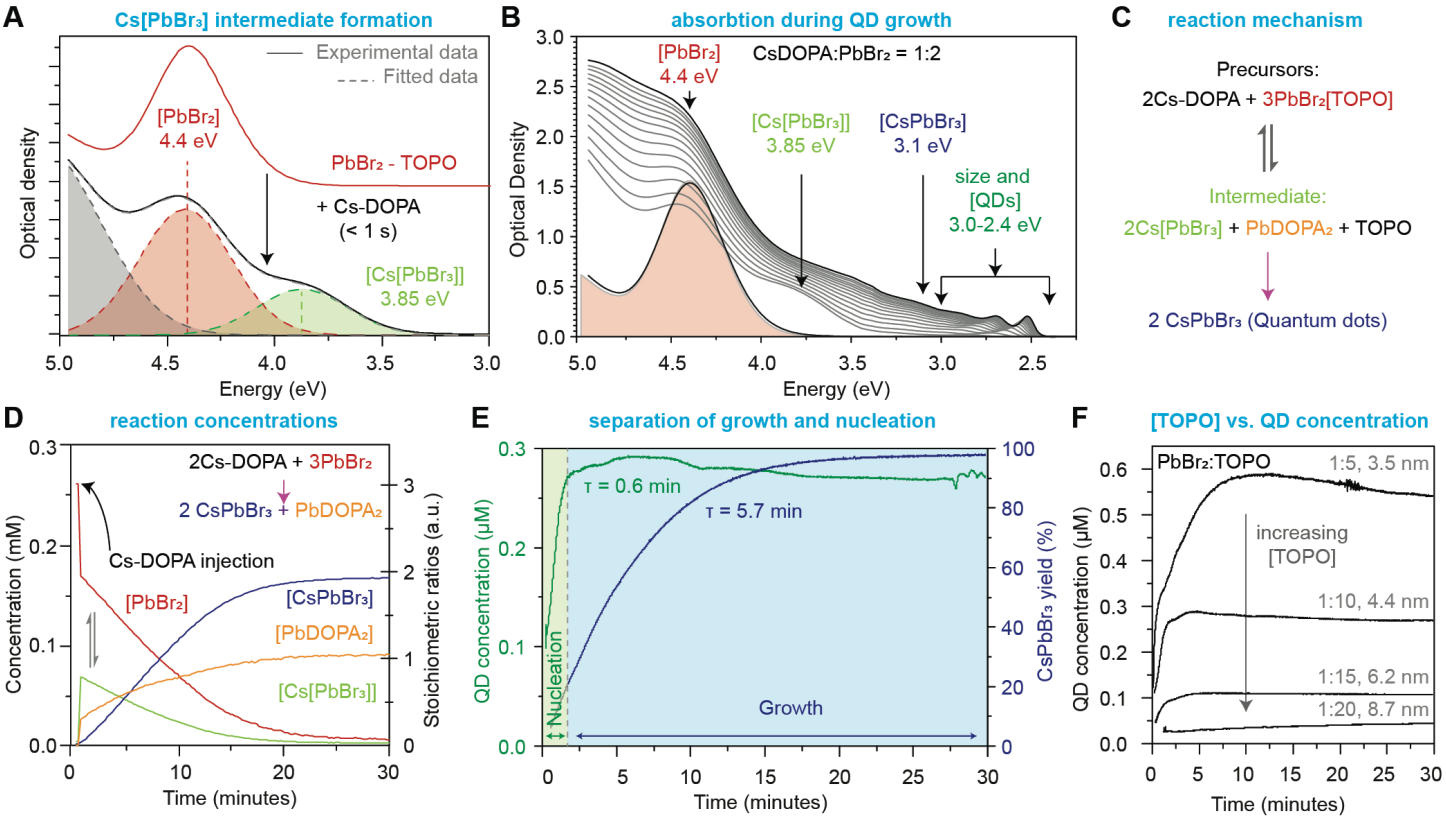

https://www.science.org/doi/10.1126/science.abq3616; SCIENCE 8 Sep 2022 Vol 377, Issue 6613 pp. 1406-1412

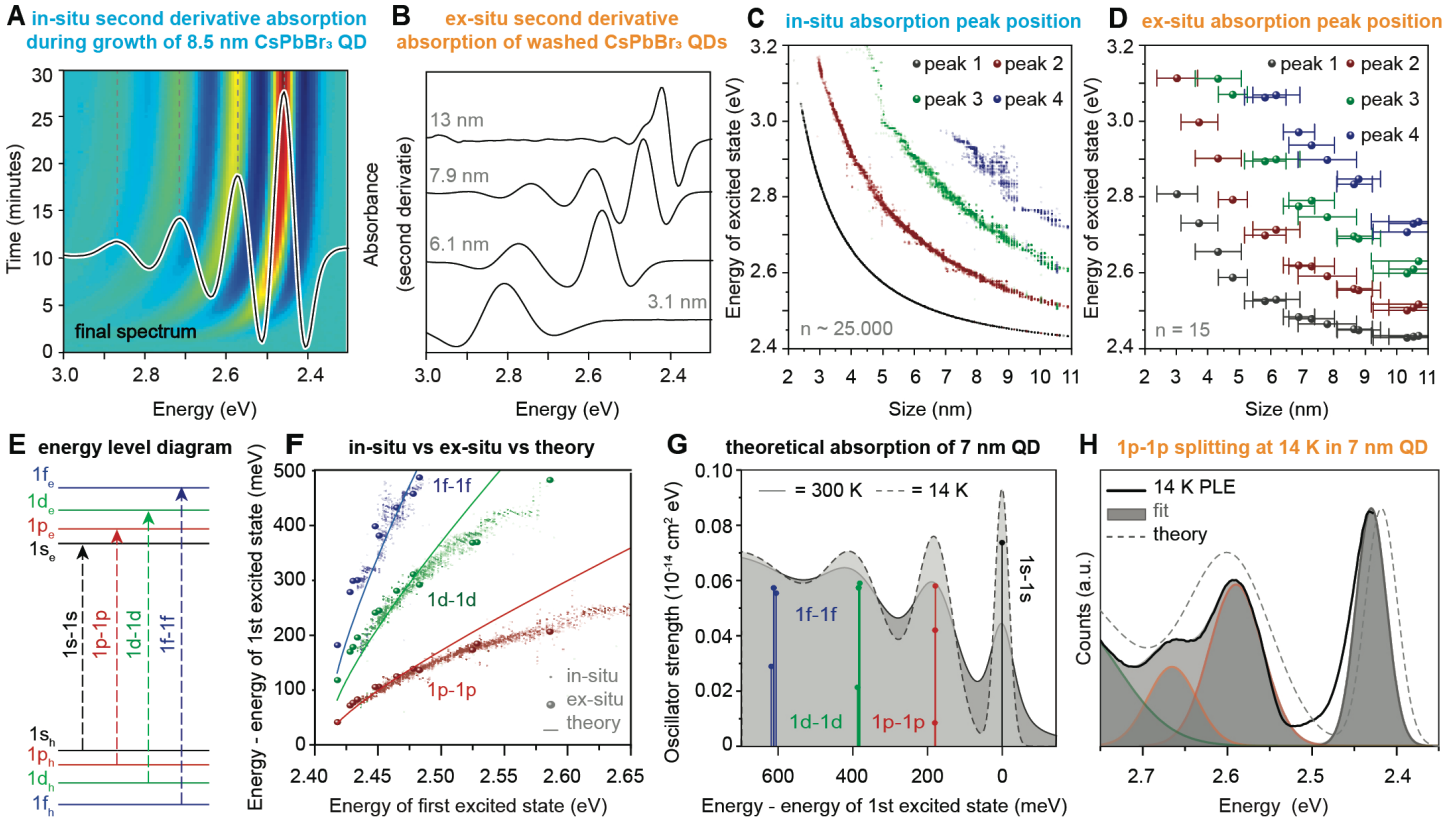

https://www.science.org/doi/10.1126/science.abq3616; SCIENCE 8 Sep 2022 Vol 377, Issue 6613 pp. 1406-1412

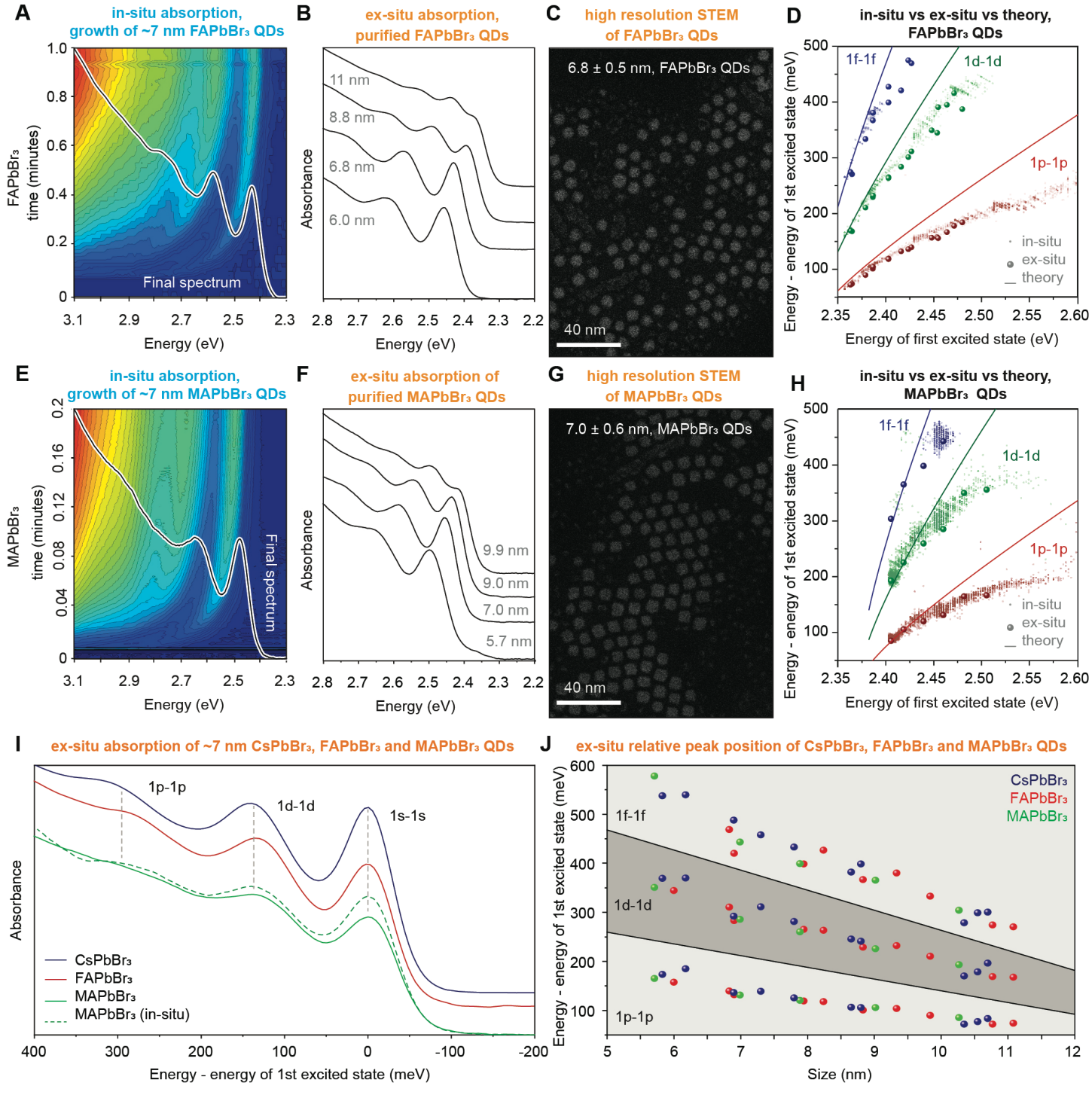

https://www.science.org/doi/10.1126/science.abq3616; SCIENCE 8 Sep 2022 Vol 377, Issue 6613 pp. 1406-1412

Supplementary Materials for

Controlling the nucleation and growth kinetics of lead halide perovskite quantum dots

Quinten A. Akkerman, Tan P. T. Nguyen, Simon C. Boehme, Federico Montanarella, Dmitry N. Dirin, Philipp Wechsler, Finn Beiglböck, Gabriele Rainò, Rolf Erni, Claudine Katan, Jacky Even and Maksym V. Kovalenko*

*Corresponding author. mvkovalenko@ethz.ch

This PDF file includes:

Materials and Methods
Supplementary Text
Figs. S1 to S42
Tables S1 and S2
Captions for Movies S1 to S5

Other Supplementary Materials for this manuscript include the following:

Movies S1 to S5

https://www.science.org/doi/10.1126/science.abq3616; SCIENCE 8 Sep 2022 Vol 377, Issue 6613 pp. 1406-1412

Materials and Methods

Chemicals

Lead bromide ($PbBr_2$, 99.999%), zinc chloride ($ZnCl_2$, 98%), cesium carbonate (Cs_2CO_3, 99.9%), formamidinium acetate (99%), methylamine (33 wt% in ethanol), acetic acid (99.5%), hexane (≥99%), diisooctylphosphinic acid (DOPA, 90%), oleic acid (OA, 90%) and acetone (ACE, ≥99.5%) were purchased from Sigma Aldrich. n-Octane (min. 99%) and lecithin (>97% from soy) were purchased from Carl Roth. Trioctylphosphine oxide (TOPO, min. 90%) was purchased from Strem Chemicals. All chemicals were used as received. Methyl ammonium acetate was synthesized by reacting methylamine with acetic acid as described in Ref (*43*).

Stock solutions

$PbBr_2$ stock solution (0.04 M), as well as $ZnCl_2$ solution used for anion exchange, was prepared by dissolving $PbBr_2$ or $ZnCl_2$ (1 mmol) and TOPO (5 mmol) in octane (5 mL) at 120 ºC, followed by dilution with hexane (20 mL). The Cs-DOPA solution (0.02 M) was prepared by mixing Cs_2CO_3 (100 mg) with DOPA (1 mL) and octane (2 mL) at 120 ºC, followed by dilution with hexane (27 mL). The FA-DOPA stock solution (0.02 M) was prepared by was prepared by loading formamidinium acetate (64 mg), DOPA (3 mL), OA (3 mL) and octane (5 mL) at 120 ºC, followed by dilution with hexane (20 mL). This solution was diluted further five times prior to the synthesis. The MA-DOPA stock solutions was prepared analogously to FA-DOPA solution using methylammonium acetate. The lecithin stock solution (~0.13 M) was prepared by dissolving 0.5 gram of lecithin in hexane (10 mL). This solution was diluted 10 times in the case of $FAPbBr_3$ and $MAPbBr_3$ QDs. The TOPO stock solution (0.2 M) was prepared by dissolving TOPO (4 mmol) in hexane (20 mL). The DOPA stock solution was prepared by diluting DOPA 40 times in hexane. The $ZnCl_2$ solutions used for anion solution was prepared in the same way as the $PbBr_2$ solutions, with the replaced of $PbBr_2$ with $ZnCl_2$. All stock solutions were filtered through 0.2 µL PTFE filter prior to use.

Synthesis of $CsPbBr_3$, $FAPbBr_3$ and $MAPbBr_3$ QDs

In an 8 ml vial, $PbBr_2$ and TOPO stock solutions were combined along with additional hexane. Under vigorous stirring, a desired volume of Cs/MA/FA-DOPA stock solution was injected. Specific volumes of solutions are tabulated in **Tables S1-S3** for all reactions presented in this work.

Ligand exchange and QD purification

Once the spectral evolution is plateaued at a final bandgap value, a stock solution of lecithin is added (the volume being equivalent to the A-cation stock solution used in the respective QD synthesis). After half a minute, a *ca*. 3-fold excess of an antisolvent (acetone for $CsPbBr_3$; ethyl acetate:acetonitrile 2:1 for $FAPbBr_3$, and $MAPbBr_3$) was added and the QDs were isolated by centrifuging at 19970 g for 2 minutes and redispersed in hexane.

Upscaled QD syntheses

The synthetic volume can be arbitrary scaled-up to yield preparative quantities of QDs. Particularly, conducting the QD synthesis in the volume of several hundred mL yields several hundred mg of QDs of the same optical properties, as long as concentrations of reagents are unaltered (**Table S3**). After the addition of lecithin ligand, the crude solution was concentrated by evaporating the hexane on a rotary evaporator down to 1-2 ml of residual solvent, thus recovering

https://www.science.org/doi/10.1126/science.abq3616; SCIENCE 8 Sep 2022 Vol 377, Issue 6613 pp. 1406-1412

the solvent for further use. The QDs were precipitated from the concentrated colloid by adding a 2-3-fold excess acetone.

In-situ absorption and photoluminescence (PL) setup

The reactions were carried out in a modified Thorlabs CVH100 cuvette holder. The absorption spectra were recorded with an Ocean Optics deuterium-tungsten light source (DH-2000-BAL-TTL-24V) and a Thorlabs CCS200/M spectrometer. For collecting PL spectra, a bifurcated optical fiber was used in a front-face configuration, minimizing the PL reabsorption. PL was excited with a Convoy 53 UV flashlight and recorded with a Thorlabs CCS200/M spectrometer. The time resolution in these measurements was set to 50 µs.

In-situ absorption in the UV range

For the higher-energy absorption studies (precursor formation and higher-order absorption transitions), covering both the UV range down to 200 nm, the reaction was carried out in a Jasco V670 spectrometer using a 2MAG cuvetteMIXdrive 1 cuvette stirring plate. This allowed for a time resolution of about 20 seconds per spectrum.

Ex-situ absorption and photoluminescence (PL) spectroscopy

Room-temperature PL spectra of purified QDs were recorded with a Fluorolog iHR 320 Horiba Jobin Yvon with an excitation at 350 nm. Absorption spectra were recorded on a Jasco V670 spectrometer.

Low-temperature PLE and absorption setup

PLE spectra were acquired with a Picoquant FluoTime300 fluorescence spectrometer equipped with a Xe lamp for excitation and a photomultiplier tube for detection. Monochromators, in both the excitation and detection path, serve to select and scan the excitation and emission wavelength. An ARS closed-cycle He cryostat in combination with a Lakeshore temperature controller were employed to control the sample temperature. The QD samples were spin-coated as thin films on Si/SiO_2 substrates and measured in vacuum. PLE spectra were recorded for an emission wavelength set to 35 meV with respect to the PL peak; qualitatively similar spectra were observed also when the emission wavelength was set to the PL peak. The low-temperature absorption was recorded in the same cryostat system, but with an Ocean Optics deuterium-tungsten lamp (DH-2000-BAL-TTL-24V) as white light source and a Thorlabs CCS200/M spectrometer as detector.

Data analysis and fitting

Custom-developed batch analysis scripts (written in Python) were employed. Here, the low-energy portion of both the absorption and PL spectra were fitted with a partial Gaussian to extract the first absorption and PL peak positions. The first absorption peak position was used to calculate the size (*21*). The molar concentration of $CsPbBr_3$ was calculated from the absorbance at 3.1 eV (*44*). The precursor concentrations were calculated by fitting the absorption data with Gaussians at 4.4 eV ($PbBr_2$) and 3.85 eV ($PbBr_3^-$) after a $CsPbBr_3$ background subtraction. The concentration of $Pb(DOPA)_2$ was determined by subtracting the $PbBr_2$, $PbBr_3^-$ and $CsPbBr_3$ concentration from the starting $PbBr_2$ concentration. The higher-order absorption transitions were determined via a peak finding function on the negative second derivative of the absorption spectra. Further details are given in the Supplementary text.

https://www.science.org/doi/10.1126/science.abq3616; SCIENCE 8 Sep 2022 Vol 377, Issue 6613 pp. 1406-1412

Small and wide-angle X-ray scattering (SAXS/WAXS) measurements

The SAXS/WAXS experiment was performed at beamline P21.2 at Petra III (DESY) synchrotron in Hamburg. X-ray photon energies of 37.5 keV (0.0331 nm) with VAREX XRD4343CT detector and a sample-to-detector distance of 1.5 m (for WAXS) and 15 m (SAXS) were employed. These distances allowed us to probe a q-range between 16 nm^{-1} and 58 nm^{-1} for the WAXS and between 0.15 nm^{-1} and 2.2 nm^{-1} for the SAXS. The q-range and the scattering intensity were calibrated with LaF_6, while absolute intensities were obtained by calibrating with glassy carbon.

For the analysis of the SAXS data, we first fitted the scattering pattern assuming a spherical form factor and a Gaussian distribution of the size (*45*). The scattering intensity is therefore expressed by the formula (*S*1):

$$I(q) = c_{NC,tot} N_A P_{sphere}(q, R) \quad (S1)$$

Where, $c_{NC,tot}$ is the molar concentration of nanocrystals, N_A is the Avogadro number and $P_{sphere}(q)$ is the isotropic scattering form factor of a spherical scattering object, which is given by formula (*S*2):

$$P_{sphere}(q, R) = 36\pi\Delta\rho^2 V_{sphere}^2 \frac{(\sin(qR) - qcos(qR))^2}{(qR)^6} \quad (S2)$$

If we also implement the Gaussian distribution of radii R, the form factor will assume the form of formula (*S*3):

$$\langle P_{sphere}(q, R)\rangle_R = 36\pi\Delta\rho^2 \frac{1}{\sqrt{2\pi\sigma_R}} \int_0^\infty e^{-\frac{1}{2}\left(\frac{R-R_0}{\sigma_R}\right)^2} V_{sphere}^2 \frac{(\sin(qR) - qcos(qR))^2}{(qR)^6} dR \quad (S3)$$

Where R_0 is the average radius of the distribution with standard deviation σ_R and $\Delta\rho$ is the scattering contrast, defined as the difference in the scattering length density of the nanocrystals and the solvent by formula (*S*4):

$$\Delta\rho = \rho_{CsPbBr_3} - \rho_{solvent} \quad (S4)$$

The scattering length densities were obtained from the Centre for X-ray Optics (CXRO, https://henke.lbl.gov/optical_constants/) as $\rho_{CsPbBr_3} = 3.1\ 10^{-5}$ Å^{-2} and $\rho_{solvent} = 4.5\ 10^{-6}$ Å^{-2} at 37.5 keV and 25 °C. This results in a scattering contrast of $2.6\ 10^{-5}$ Å^{-2}.

The assumption of pseudo spherical particles was confirmed by independently fitting (i.e. without any prior assumption on the morphology) the experimental data with a commercially available shape retrieval algorithm based on dummy atoms (SasHel) (*46*). The reconstructed average morphology of the scattering objects is pseudo spherical with one axis slightly shorter than the other two.

Transmission electron microscopy measurements (TEM)

TEM images were obtained using a JEOL JEM-1400 Plus microscope operating at 120 kV. Bright-field and dark-field scanning TEM (STEM) imaging was performed on a JEOL JEM2200FS microscope equipped with a Schottky field emission electron gun. High-angle annular dark-field scanning TEM (HAADF-STEM) images were collected at cryo-conditions (holder cooled with liquid nitrogen) on an aberration-corrected HD2700CS (Hitachi) operated at 200 kV

https://www.science.org/doi/10.1126/science.abq3616; SCIENCE 8 Sep 2022 Vol 377, Issue 6613 pp. 1406-1412

with a point resolution of ca. 1 Å. HR ADF-STEM was carried out using a probe-aberration-corrected FEI Titan Themis operated at 300 kV employing a beam semi-convergence angle of 18 mrad and a beam current of 1 pA. Under the high-resolution acquisition conditions used, the dose per frame was about 50 electrons/Å^2. Series of images of each particle were recorded and 8-10 frames were averaged for noise-reduction, warranting that the nanoparticles remained unchanged in the averaged frames. The frames were aligned using the non-rigid algorithm as implemented in SmartAlign (*47*).

Empirical modelling

For the comparison between a sphere and a cube, EMA was employed together with a single-shot computation of Coulomb interaction. The correspondence $L = \sqrt{3}\,R$ was made where L and R are the cube edge length and sphere radius, respectively. For the peak assignment and the absorption cross-section, assuming spherical symmetry, the two-band $k.p$ model was used and the Coulomb interaction was treated using the Hartree-Fock approximation. Electron-photon interaction was computed within second-order many-body perturbation theory. The QD size is taken to be $\sqrt{3}\,R_{eff}$ where R_{eff} is the effective sphere radius. More details can be found in the subsequent Supplementary Text.

https://www.science.org/doi/10.1126/science.abq3616; SCIENCE 8 Sep 2022 Vol 377, Issue 6613 pp. 1406-1412

Supplementary Text

Synthesis details and parametric screening

The QD size in this work was mainly regulated by changing the overall concentration (dilution) or by adjusting the concentration of TOPO, as described in the main text. In addition, the size could be controlled also by varying the concentration of $PbBr_2$ and Cs-DOPO individually. **fig. S1** illustrates the effect varying the quantity of the $PbBr_2$ stock solution (with a fixed $PbBr_2$:TOPO ratio and fixed amount of injected Cs-DOPA solution). Larger QDs were obtained at higher $PbBr_2$ concentrations. Alternatively, keeping the $PbBr_2$ fixed and decreasing the amount of injected Cs-DOPA results in a similar trend within a Pb:Cs ratio of 2-8, wherein higher Cs-DOPA concentration results in larger QDs, as shown in **fig. S2**. Above the 8:1 Pb:Cs ratio, the concentration of Cs-DOPA does not seem to alter the final size of the QDs. Decreasing the Pb:Cs ratio to below 2:1 will lead to the formation of the Cs_4PbBr_6 phase, as is evident from the strong absorption around 3.95 eV, as shown in **fig. S3**. Finally, the increase of the DOPA concentration in the Cs-DOPA precursor, and therefore the increase of free DOPA ligands during the reaction, does not have a significant effect on the final size and growth speed of $CsPbBr_3$ QDs, as shown in **fig. S4**. The reproducibility of this room-temperature $CsPbBr_3$ synthesis is illustrated in **fig. S5**, wherein a specific reaction is repeated four times (800 µl $PbBr_2$ stock solution, 50 µl Cs-DOPA stock solution and 5000 µl hexane). All four reactions yield the same growth curve, with a standard deviation in the final size of just 2%. Similar values are found for the peak FWHM and the PL peak position.

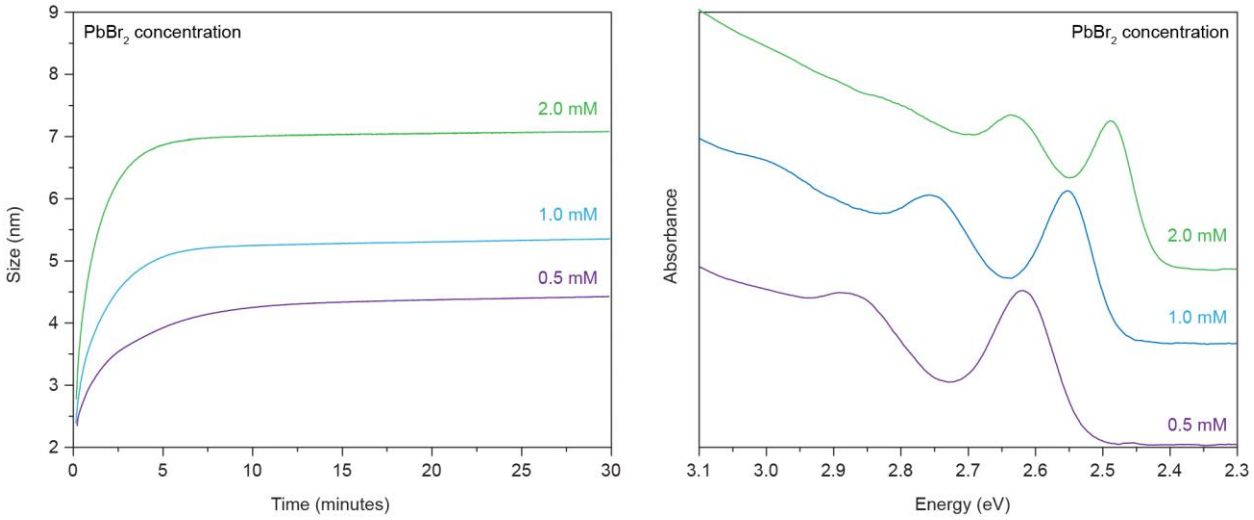

Fig. S1. $CsPbBr_3$ QD size-control by varying the $PbBr_2$ precursors with a fixed Cs-DOPA concentration, showing larger QDs and faster reactions with increasing $PbBr_2$ concentration.

https://www.science.org/doi/10.1126/science.abq3616; SCIENCE 8 Sep 2022 Vol 377, Issue 6613 pp. 1406-1412

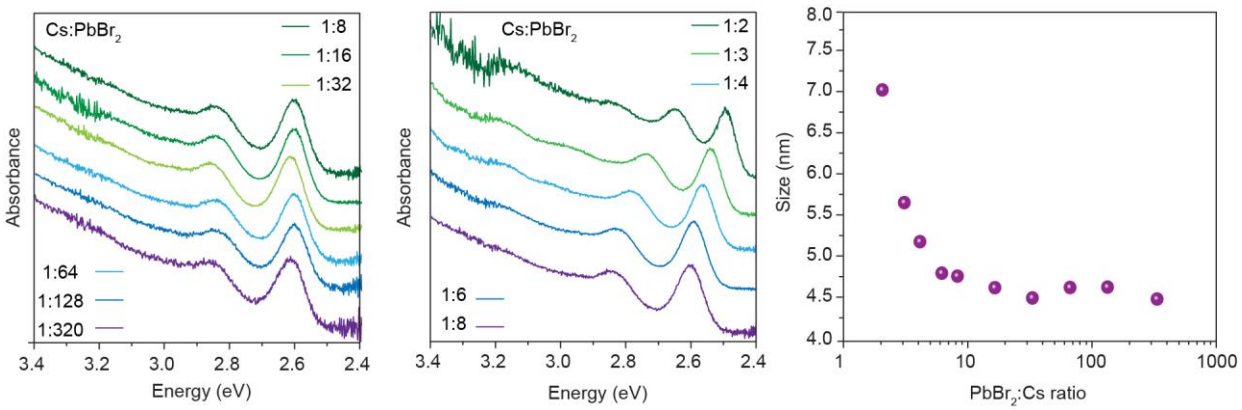

Fig. S2. Effect of Cs:Pb molar precursor ratio, showing no effect on the QD size at very large Pb excess, and a convenient size-tuning for ratios between 1:8 and 1:2.

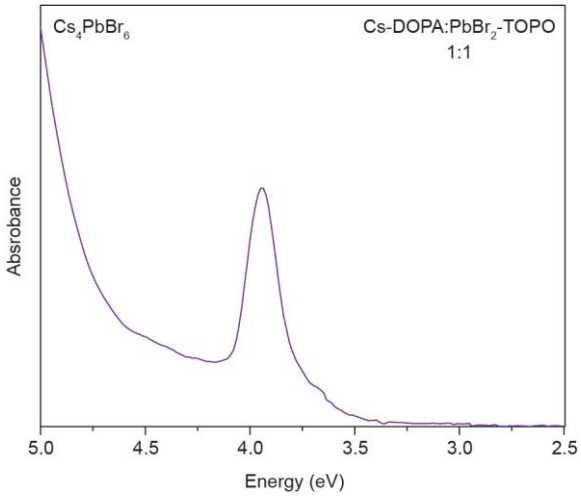

Fig. S3. Formation of Cs_4PbBr_6, characterized by the narrow absorption at 3.95 eV (*48*), at a Cs to Pb ratio of 1:1.

https://www.science.org/doi/10.1126/science.abq3616; SCIENCE 8 Sep 2022 Vol 377, Issue 6613 pp. 1406-1412

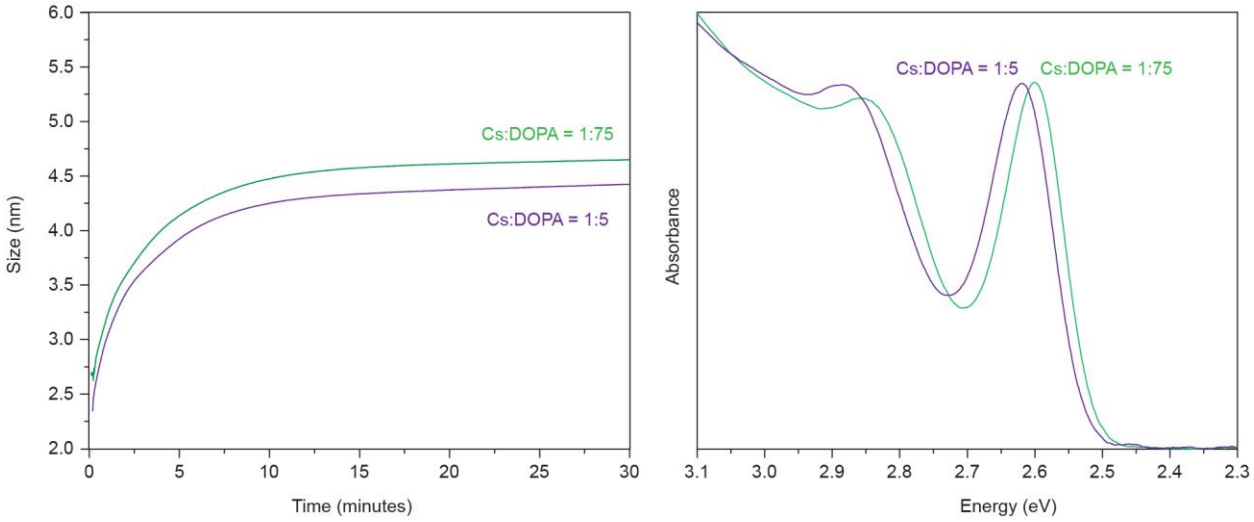

Fig. S4. Experiments with the high excess of DOPA acid, with keeping all other reaction conditions fixed, demonstrating that excess DOPA does not influence the growth of $CsPbBr_3$.

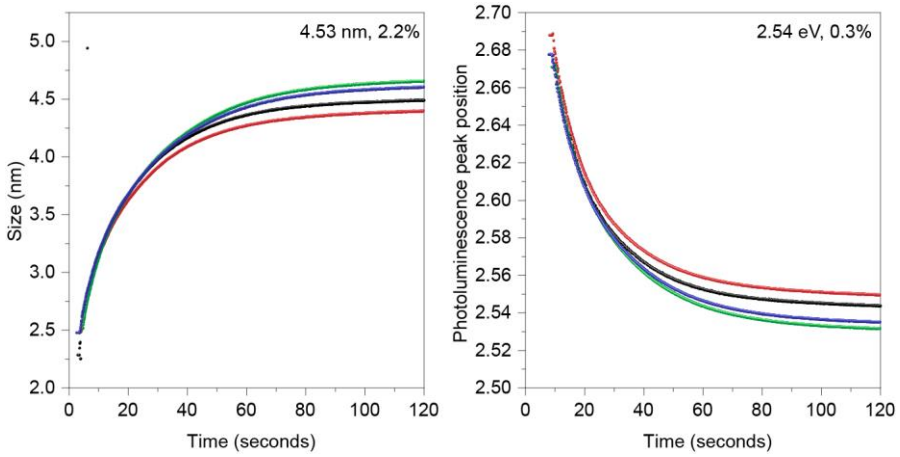

Fig. S5. Reproducibly of $CsPbBr_3$ QD synthesis confirmed by repeating the same synthesis four times.

In-situ data analysis

Due to the large number of spectra (> 1000 per synthesis), Python scripts were used to extract absorption peak positions, first absorption peak FWHM, as well as PL peak positions and FWHM. The first absorption peak position and its respective FWHM were smoothed (Savitzky–Golay) and fitted with a partial Gaussian fit. Here, the Gaussian was fully fitted at low energies (up to 2.1 eV) and partially at high energies. From the fitted Gaussian, the first absorption peak position and FWHM were extracted. Similarly, the PL data was smoothed (Savitzky–Golay) and fitted with a Gaussian. Due to the asymmetry of the PL, the Gaussian was fully fitted at high energies (up to 3.1 eV nm) and partially at low energies. This allowed for a better determination of the peak position. From the fitted Gaussian, the PL peak position was extracted. The Stokes shift data were calculated by subtracting the PL peak position from the absorption peak position as determined from the fitted Gaussians. An example of a fitted absorption and PL spectra is shown in **fig. S6.** To convert to absorption bandgap of the $CsPbBr_3$ QDs into the QD size, we used the sizing curve published by Krieg *et al* (*21*). Here, the model was fitted with an exponential fit

https://www.science.org/doi/10.1126/science.abq3616; SCIENCE 8 Sep 2022 Vol 377, Issue 6613 pp. 1406-1412

(Belehradek, which gave the best fit), as shown in **fig. S7A**. This model fits well with the experimentally determined size via TEM of the spheroidal QDs presented in this work (**fig. S7B**).

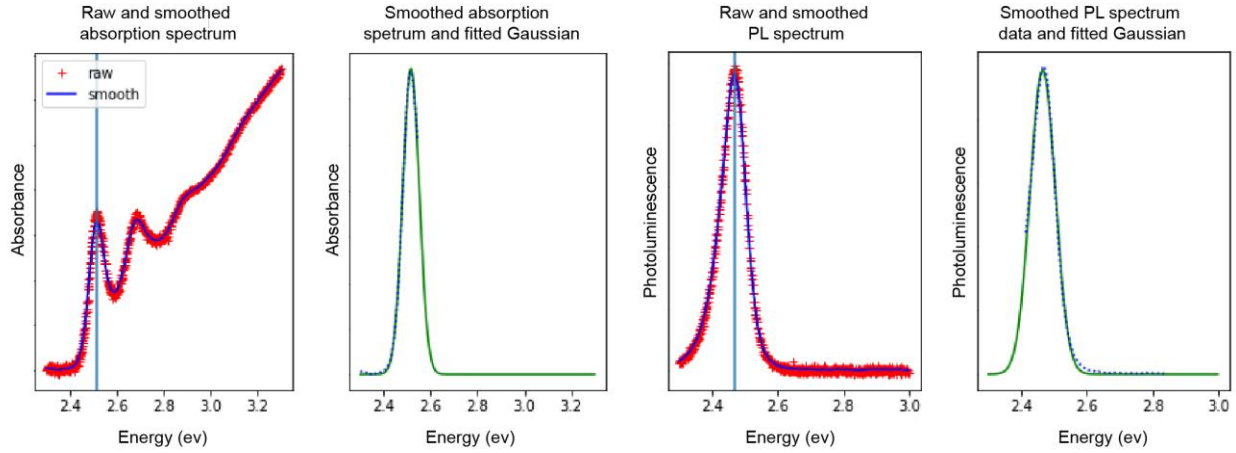

Fig. S6. Example of Gaussian fitting of absorption and PL data.

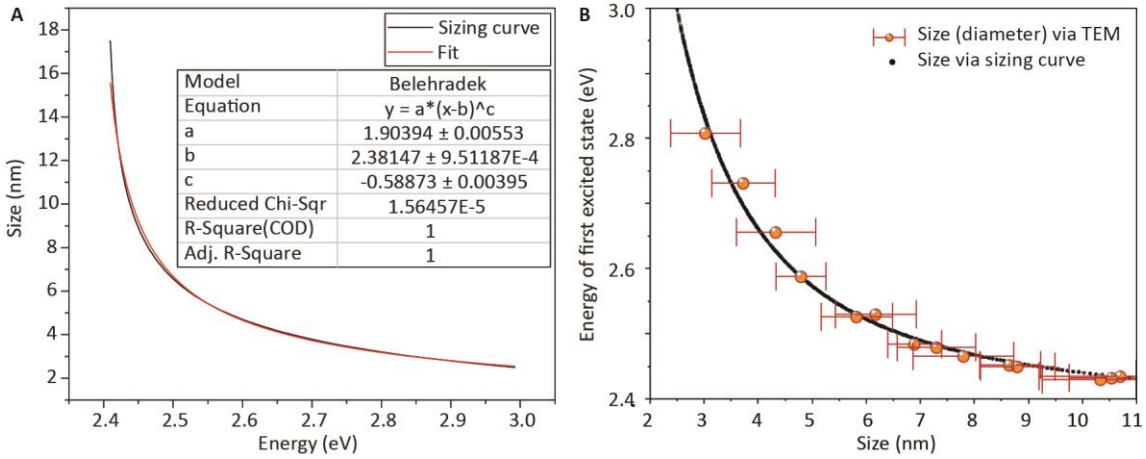

Fig. S7. **A,** Sizing curve used to convert the bandgap value into the QD size. **B,** Comparison with the experimental bandgap vs. QD diameter (from TEM) dependency.

The final yield and QD concentration of the $CsPbBr_3$ reactions was calculated by using the optical density at 400 nm which, combined with the intrinsic absorption coefficient (size-independent at high photon energies), allowed for the determination of the overall $CsPbBr_3$ concentration (in molarity) (*44*). The yield of the reaction was determined based on the initial Cs^+ concentration, which in all reactions was the limiting precursor. The QD concentration was calculated via the $CsPbBr_3$ concentration, and presuming a spherical shaped QD with the size extracted from the first excitonic transition as described above. The higher order absorption peaks, as shown in **Fig. 4** and **Fig.5,** were extracted from the negative second derivative of the absorption spectra. Here, absorption spectra were smoothed (Savitzky–Golay), followed by the calculation of the second derivative. The second derivative was further smoothed and a *peak_find* function was used to determine the final absorption peak positions. This process is shown in **fig. S8.** To confirm the error of the extracted properties, we performed an in-situ measurement with the same acquisition time as a growth time but with a pre-synthesized, purified sample. As shown in **fig. S9**, the standard deviation of the extracted absorption and PL peak positions is extremely low (0.02-

https://www.science.org/doi/10.1126/science.abq3616; SCIENCE 8 Sep 2022 Vol 377, Issue 6613 pp. 1406-1412

0.04%, n = 1800). This error translates into a standard deviation of about 2% for the Stokes shift. As with the fitting of the bandgap, the extracted higher order peak positions have a standard deviation on the order of 0.001-0.4%.

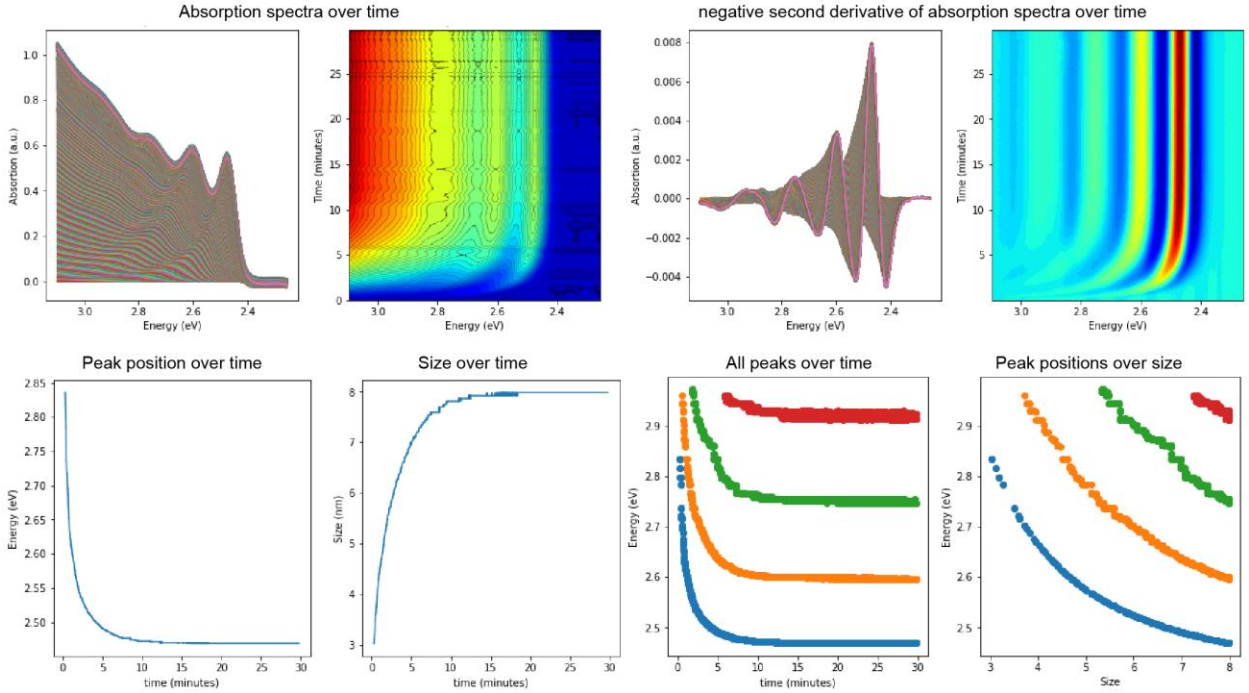

Fig. S8. Example of higher-order excitonic peak finding using second derivative.

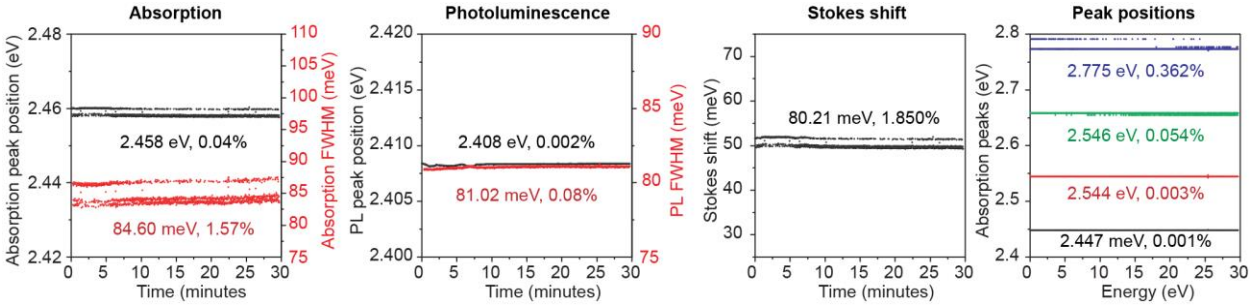

Fig. S9. Standard deviations of data extraction.

https://www.science.org/doi/10.1126/science.abq3616; SCIENCE 8 Sep 2022 Vol 377, Issue 6613 pp. 1406-1412

Calculations of the absorption spectra of perovskite QDs

Let M_{eh} be the reduced amplitude of the electron-photon matrix element (*38*). The one-photon absorption cross-section at energy E can be evaluated by summing over all allowed transitions as follows

$$\sigma^{(1)}(E) = \frac{4\pi^2}{3} \frac{f_\varepsilon^2}{\sqrt{\varepsilon_{out}}\, c_0} \sum_{eh} \frac{1}{E_{eh}} |M_{eh}|^2 \; g_{eh}(E - E_{eh}). \quad (S5)$$

In the above expression, c_0 is the speed of light in vacuum and $\frac{f_\varepsilon^2}{\sqrt{\varepsilon_{out}}}$ is the dielectric screening factor, which is taken to be the same for a cube and a sphere in the current calculation with $f_\varepsilon = \frac{3\varepsilon_{out}}{\varepsilon_{in} + 2\,\varepsilon_{out}}$. The value of ε_{in} is assumed to be the optical dielectric constant, which can be quite different from the effective dielectric constant ε_{eff} used for the Coulomb interaction. Each transition is broadened by a normalized line-shape function $g_{eh}(E - E_{eh})$, for which a further discussion can be found in the supplementary text.

Effective Mass Approximation (EMA)

To compare absorption spectra of the spheroidal and cuboidal QDs, the EMA was used in which the envelope part of the total wave function is decoupled from the Bloch degree of freedom. Under the separation of length scales, the Bloch part, which varies on the atomic scale, can be integrated out leaving only the expressions for the envelope functions to be dealt with. The theoretical details for the cubic QD, to which the spherical case is similar, can be found below.
In the cubic confining potential that is given as

$$V_{\text{conf}}^{\text{cube}}(\vec{r}) = \begin{cases} 0, \text{ if } |i| < \frac{L_i}{2} \text{ for any } i = x, y, z, \\ \infty, \quad \text{otherwise,} \end{cases} \quad (S6)$$

the noninteracting single-particle wave function of the envelope part is

$$\psi_{n_x n_y n_z}^{\text{cube}}(\vec{r}) = \sqrt{\frac{8}{L_x L_y L_z}} \cos\left(\pi n_x \frac{x}{L_x} - \phi_{n_x}\right) \cos\left(\pi n_y \frac{y}{L_y} - \phi_{n_y}\right) \cos\left(\pi n_z \frac{z}{L_z} - \phi_{n_z}\right). \quad (S7)$$

The quantum numbers n_x, n_y, n_z are positive integers and their phase factors are defined as $\phi_{n_i} = \frac{\pi}{2}\, mod(n_i + 1,2), i = x, y, z$. The corresponding single-particle energy of the state in Eq. $(S7)$ is

$$E_{\text{conf}}^{\text{cube}}(n_x, n_y, n_z) = \frac{\hbar^2 \pi^2}{2m^*} \frac{1}{L^2} \left(\frac{n_x^2}{b_x^2} + \frac{n_y^2}{b_y^2} + n_z^2\right). \quad (S8)$$

We note that the solution above is for a more general case where the QD shape is a rectangle cuboid of which the confining potential $V_{\text{conf}}^{\text{cube}}(\vec{r})$ is given as in Eq. $(S6)$. The ratios $b_x = L_x/L$ and $b_y = L_y/L$ (with $L_z = L$) describe the degree of shape anisotropy of the cuboidal QD. The three-

https://www.science.org/doi/10.1126/science.abq3616; SCIENCE 8 Sep 2022 Vol 377, Issue 6613 pp. 1406-1412

tuple of quantum numbers (n_x, n_y, n_z) provides information on the symmetry of the state. In particular, the cubic state $(n_x, n_y, n_z) = (1,1,1)$ is equivalent to the spherical $1s$ state. Similarly, $(n_x, n_y, n_z) = (2,1,1)$, $(1,2,1)$ and $(1,1,2)$ correspond to $1p_x$, $1p_y$ and $1p_z$, respectively. In the isotropic case, i.e. $b_x = b_y = 1$, the three $1p$ states are exactly degenerate, resulting in the same degeneracy equal to three as for the spherical $1p$ states. The relative energy difference between a sphere and an isotropic cube is around a few percent at most. For each optical transition allowed to the single exciton state $|eh\rangle = \psi^{\text{cube}}_{n_x n_y n_z}(\vec{r}_e)\, \psi^{\text{cube}}_{n'_x n'_y n'_z}(\vec{r}_h)\, a_c^\dagger a_v\, |\emptyset\rangle$ ($a^\dagger/a$ stands for the fermion creation/annihilation operator and $|\emptyset\rangle$ denotes the semiconductor ground state), the Coulomb interaction was computed using the single-particle wave function, Eq. $(S7)$,

$$E^{\text{cube}}_{\text{Coul}}(n_x, n_y, n_z;\ n'_x, n'_y, n'_z) = \iint \psi^{*\text{cube}}_{n'_x n'_y n'_z}(\vec{r}_h)\, \psi^{*\text{cube}}_{n_x n_y n_z}(\vec{r}_e)\, V(\vec{r}_e, \vec{r}_h)\, \psi^{\text{cube}}_{n_x n_y n_z}(\vec{r}_e)\, \psi^{\text{cube}}_{n'_x n'_y n'_z}(\vec{r}_h)\, d\vec{r}_e\, d\vec{r}_h\ . \quad (S9)$$

Given that ε_{eff} is the effective dielectric constant of the QD material, the long-range Coulomb interaction $V_{12} = V(\vec{r}_1, \vec{r}_2)$ can be written as

$$V(\vec{r}_1, \vec{r}_2) = \frac{1}{\varepsilon_{eff}\, |\vec{r}_1 - \vec{r}_2|}\ . \quad (S10)$$

For a material with electronic band gap E_{gap}, the energy E_{eh} of a single exciton confined in a cubic QD is, thus,

$$E^{\text{cube}}_{eh} = E_{\text{gap}} + E^{\text{cube}}_{\text{conf}}(n_x, n_y, n_z) + E^{\text{cube}}_{\text{conf}}(n'_x, n'_y, n'_z) + E^{\text{cube}}_{\text{Coul}}(n_x, n_y, n_z;\ n'_x, n'_y, n'_z). \quad (S11)$$

The energy E^{cube}_{eh} contains the Coulomb interaction from a single-shot computation without self-consistency iteration and wave function relaxation. The single-shot computation of $E^{\text{cube}}_{\text{Coul}}$ seems to suffice for the current purpose of comparing the cubic and spherical absorption spectra.

The final input to the expression for the single-photon absorption cross-section $\sigma^{(1)}$ is the transition amplitude M_{eh}, which take the following simple expression in the EMA,

$$|M_{eh}|^2 = E_P\, \delta_{n^e_x n^h_x}\, \delta_{n^e_y n^h_y}\, \delta_{n^e_z n^h_z}. \quad (S12)$$

The Kane parameter E_P is directly related to the optical matrix element between the lowest conduction and highest valence bands. Before being broadened with a line-shape function to obtain $\sigma^{(1)}$, the expression $\Xi_{eh} = \frac{4\pi^2}{3} \frac{f_\varepsilon^2}{\sqrt{\varepsilon_{out}}\, c_0} \frac{1}{E_{eh}} |M_{eh}|^2$ is sometimes referred to as the oscillator strength for the transition from the ground state $|\emptyset\rangle$ to the exciton state $|eh\rangle$.

The spherical calculations used the same method and numerical code. At this level of theory, the conduction-valence band coupling was turned off by setting the Kane parameter to 0 in the $k.p$ Hamiltonian. As a useful remark, the spherical transition amplitude M_{eh} satisfies

$$|M_{eh}|^2 = E_P\, \delta_{l_e l_h}\, \delta_{m_e m_h} \delta_{n_e n_h}, \quad (S13)$$

where n_e and n_h are the principal quantum numbers of the electron and hole states. The above selection rule implies that the only optically allowed transitions in EMA are $1s - 1s, 1p -$

https://www.science.org/doi/10.1126/science.abq3616; SCIENCE 8 Sep 2022 Vol 377, Issue 6613 pp. 1406-1412

$1p, 1d - 1d$, etc. named according the various spherical angular momenta and principal quantum numbers. Strictly speaking, this is no longer true for the $k.p$ model even though these transitions remain the ones giving major contributions.

To make a fair comparison between a cube and a sphere, we used the following relation between the sphere radius R and the cube edge length L where

$$L = \sqrt{3}\, R. \tag{S14}$$

Relation $(S14)$ was chosen such that the lowest noninteracting single-particle energies (i.e. of the $1s$ state) of an isotropic cuboid and the equivalent sphere are identical. In fact, this relation leads to the entire s-series energies to coincide for both geometries, see formulae $(S8)$ and $(S15)$.

$$E_{\text{conf}}^{\text{sph}}(n, l = 0) = \frac{\hbar^2 \pi^2}{2m^*} \frac{n^2}{R^2}\,. \tag{S15}$$

Besides, it turns out that the computed Coulomb interacting energies, without self-consistency, for the $1s$ come out to be very similar to the one of a cube, having a relative difference of around a few percent from one another. Thus, the relation $(S14)$ is justified for the comparative study between the spherical and cubic absorption spectra. Using this relation between L and R, one can arrive at the conclusion that the excitonic features are more pronounced in a sphere than its equivalent cube, as discussed in the main text.

Two-band $k.p$ model and Hartree-Fock approximation

Due to large spin-orbit splitting in lead halide perovskites, the band edges at the R-point of the Brillouin zone consist of an $p_{1/2}$-like conduction and a s-like valence band with R_6^- and R_6^+ symmetries respectively. (s and p refer to the orbital angular momenta of the Bloch functions). Therefore, the two-band $k.p$ model (also known as 4×4 $k.p$ model) is well-suited to describe the dispersion of electrons and holes around the R-point. In particular, we considered here the spherically symmetric $k.p$ Hamiltonian $H_{k.p}$. In a spherical confinement V_{ext}, the total angular momentum $\vec{F} = \vec{l} + \vec{J}$ is a conserved quantity, where $\vec{l}$ is the orbital angular momentum of the envelope function and $\vec{J}$ is the angular momentum of the Bloch part. In other words, an eigenstate of $H_{k.p}$ in the external potential V_{ext} can be written as

$$|\eta F m_F\rangle = \frac{\mathcal{R}_s(r)}{r} \left|\left(l, \frac{1}{2}\right) F m_F\right\rangle + \frac{\bar{\mathcal{R}}_p(r)}{r} \left|\left(\bar{l}, \frac{1}{2}\right) F m_F\right\rangle, \tag{S16}$$

where $\mathcal{R}_s(r)$ and $\bar{\mathcal{R}}_p(r)$ are the radial components of the envelope wave functions corresponding to the s-like and $p_{1/2}$-like bands, respectively (*49*).

At mean-field level, the Coulomb interaction between the charge carriers can be approximated using the Hartree-Fock (HF) potential. The HF equation for an occupied state $|a\rangle$ (i.e. a state with a charge present) is defined to be

$$\left(H_{k.p} + V_{\text{conf}}^{\text{sph}} + V_{HF}^{av}\right) |a\rangle = \epsilon_a |a\rangle. \tag{S17}$$

https://www.science.org/doi/10.1126/science.abq3616; SCIENCE 8 Sep 2022 Vol 377, Issue 6613 pp. 1406-1412

The first two terms give rise to the confined kinetic energy of a carrier trapped inside the QD. The third term $V_{HF}^{av} = V_{dir} + V_{exc}$ is the spherically averaged HF potential, which is the sum of the direct and exchange interaction over all occupied electron and hole states $|b\rangle$. Explicitly,

$$\begin{aligned} \langle i|V_{dir}|a\rangle &= \sum_{b}^{occ} e_b q_b^a \langle ib|V_{12}|ab\rangle , \\ \langle i|V_{exc}|a\rangle &= -\sum_{b}^{occ} e_b q_b^a \langle ib|V_{12}|ba\rangle , \end{aligned} \tag{S18}$$

where $|a\rangle, |b\rangle, \ldots$ denote the occupied states and $|i\rangle$ is any arbitrary state (occupied and unoccupied). We followed the charge convention $e_b = 1$ and -1 for electron and hole, respectively (*49*). The weight q_b^a represents the averaged occupation of a shell B, containing the state $|b\rangle$, relative to the state $|a\rangle$ in shell A. Additional details of the $k.p$ model and the HF formalism can be found in reference (*49*). We briefly note that the current formalism can be used to describe, at the HF (mean-field) level, systems of N_e electrons and N_h holes, subsuming the case of a single exciton but not only. Letting q_a be the fractional occupation of shell A, the HF energy of the aforementioned system is

$$E_{HF}^{av} = \sum_{a}^{occ} e_a q_a \left\langle a\middle|H_{k.p} + V_{\text{conf}}^{\text{sph}}\middle|a\right\rangle + \frac{1}{2}\sum_{a}^{occ} e_a q_a \langle a|V_{HF}^{av}|a\rangle . \tag{S19}$$

The HF energy is useful for estimating the energy needed to add or remove a particle (electron or hole) from the system, which can be regarded as the Koopmans' theorem for the envelope degree of freedom.

Most importantly, the HF potential can be used to generate a complete basis set, called the HF basis set, that can be used, for instance, in the many-body calculations for the electron-photon interaction and other correlation corrections (*38, 49*). Here, we only summarize the important conclusions while the details of second-order many-body perturbation theory for one-photon absorption can be found in reference (*49*). The interband electron-photon matrix elements receive a significant correction from correlation effects. An enhancement of the lower excitonic transitions has been demonstrated to improve the shape of the absorption curve. Notably, the lowest $1s - 1s$ exciton receives a large correction factor, which is directly linked to the sub-nanosecond radiative lifetime at cryogenic temperature (*49*). For these reasons, the second-order many-body perturbation theory was employed for the calculation of the cross-section $\sigma^{(1)}$ as shown in **Fig. 4g** of the main text.

Finally, we discuss the parameters used in these empirical methods. The fundamental input parameters that are the reduced effective mass $\mu = 0.126$ and effective dielectric constant $\varepsilon_{eff} = 7.3$ are taken from Yang *et al* (*50*). for $CsPbBr_3$. The electron and hole effective masses were assumed to be equal leading to $m_e^* = m_h^* = 2\mu$. From the deduced m_e^* and m_h^*, the input $m^* = m'$ in Eq. $(S8)$ and Eq. $(S15)$ is obtained from applying the formula for the energy-dependent effective mass m' in reference (*32*). The electronic band gap is set to be $E_{\text{gap}} = 2.424$ eV, which is consistent with the value used in Krieg *et al* (21). For $FAPbBr_3$ and $MAPbBr_3$, the reduced effective mass μ and effective dielectric constant ε_{eff} are taken from Galkowski *et al* (*51*). The

https://www.science.org/doi/10.1126/science.abq3616; SCIENCE 8 Sep 2022 Vol 377, Issue 6613 pp. 1406-1412

value for the Kane parameter E_P was chosen to be $E_P = 20.0$ eV for all three A-site cations (*49*). Note that this conservative value lies in between the various estimates coming from the two-band and four-band $k.p$ models. Again, additional information is required to correctly assess the actual value of E_P, which we leave for future work. The EMA in spherical geometry can be obtained by switching off the conduction-valence band coupling (i.e. setting $E_P = 0$) in the $k.p$ Hamiltonian while keeping the optical matrix element, which is proportional to $\sqrt{E_P}$, nonzero.

Additional mechanistic studies.

To accurately calculate the concentration of the $PbBr_2$ and $PbBr_3^-$ precursors during the growth, we firstly determined their respective molar absorption coefficient as shown in **fig. S10.** Here, the molar absorption coefficient of the $PbBr_2$[TOPO] complex was determined by measuring the optical density at 4.4 eV of solutions with different concentration of $PbBr_2$[TOPO] in hexane. For the molar absorption coefficient of $PbBr_3^-$, a small excess of didodecyldimethylammonium bromide (DDAB, 98%, purchased from Sigma Aldrich) dissolved in chloroform ($CHCl_3$, 99.8%, purchased from Sigma Aldrich) was added to the $PbBr_2$[TOPO] solutions. This resulted in the $PbBr_3^-$ absorption band appearing at 3.85 eV, matching that of the one measured for the Cs[$PbBr_3$] complex.

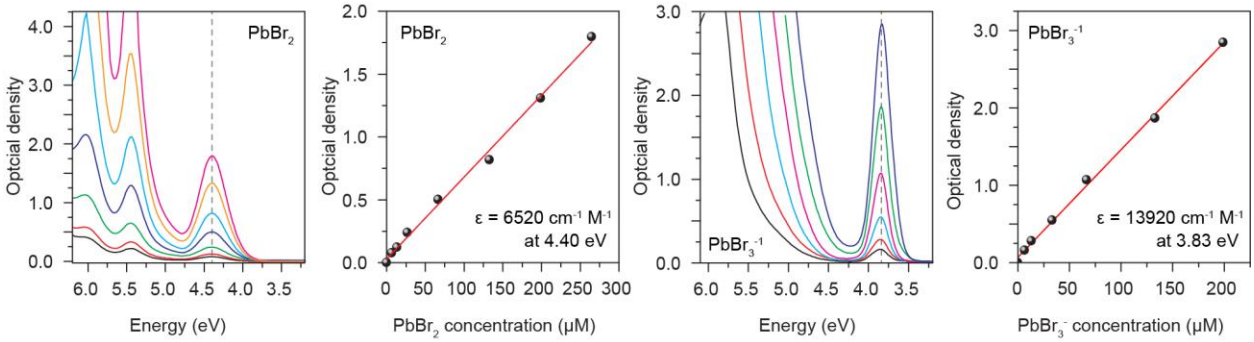

Fig. S10. Determination of molar extension coefficients of $PbBr_2$ and Cs[$PbBr_3$]TOPO complexes in hexane.

To determine the $PbBr_2$, $PbBr_3^-$, $CsPbBr_3$ and $PbDOPA_2$ concentration in-situ, we firstly determined the concentration of $CsPbBr_3$ at 3.1 eV, based on the reported extinction coefficient by De Roo *et al* (*44*). Due to the absorption onset of the growing $CsPbBr_3$ QDs, we subtracted an absorption spectrum of large washed $CsPbBr_3$ QDs scaled to the absorption at 3.1 eV; this process is shown in **fig. S11**. This allowed us to determine the concentration of $PbBr_2$, $PbBr_3^-$, without the absorption onset of $CsPbBr_3$. The remaining absorption spectra were fitted with Gaussians fixed at 4.4 and 3.83 eV. The resulting peak maxima of these fits were used as OD and to directly calculate the respective $PbBr_2$ and $PbBr_3^-$ concentrations. Based on the proposed reaction mechanism as shown in **Fig. 3**, we calculated the $PbDOPA_2$ concentration by extracting the $PbBr_2$, $PbBr_3^-$, $CsPbBr_3$ concentrations from the starting $PbBr_2$ quantity.

https://www.science.org/doi/10.1126/science.abq3616; SCIENCE 8 Sep 2022 Vol 377, Issue 6613 pp. 1406-1412

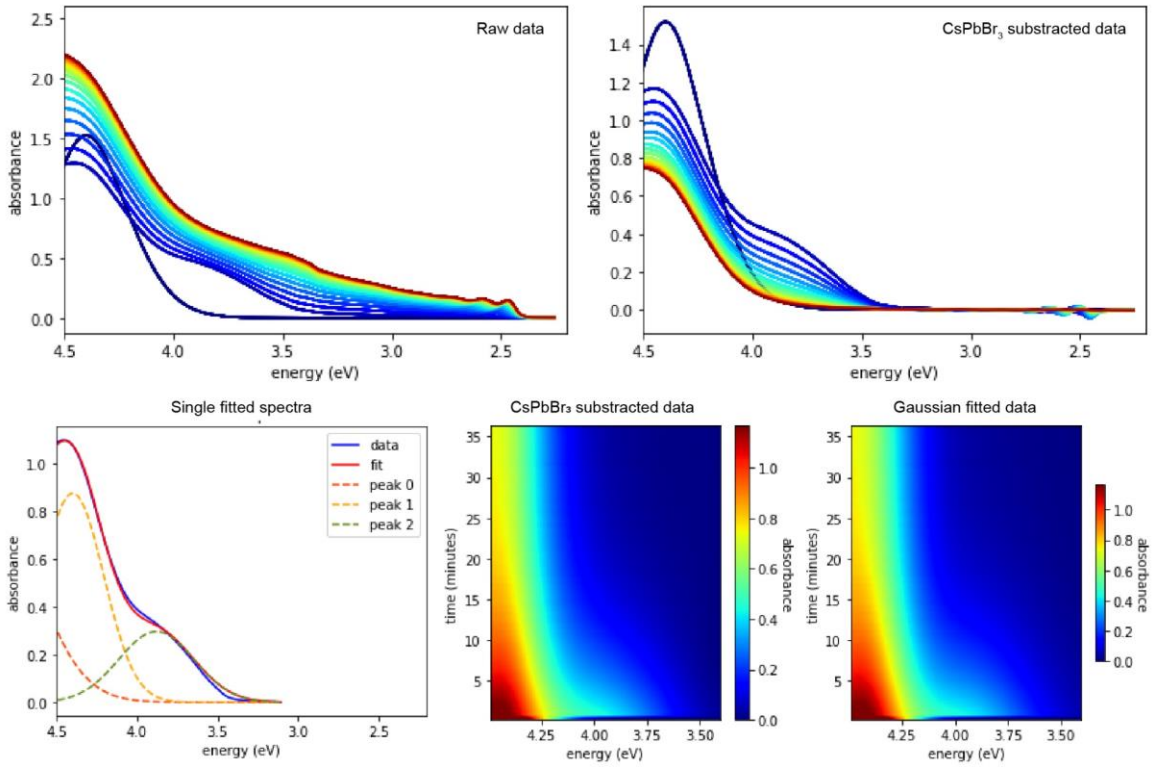

Fig. S11. Example of fitting and extraction of $PbBr_2$ and $PbBr_3^-$ concentrations.

We further confirm the $PbBr_2$:Cs[$PbBr_3$] equilibrium by shifting it towards the Cs[$PbBr_3$] side. This can be done by replacing Cs-DOPA with Cs-oleate solution with an excess of free oleic acid. As demonstrated by Almeida *et al* (*28*)., free oleic acid is strong enough to protonate TOPO and form $PbBr_3^-$ (most likely in the form of $PbBr_3$:TOPOH). As shown in **fig. S12,** replacing Cs-DOPA with Cs-OA results in the fast growth of polydisperse $CsPbBr_3$ QDs. This can be explained by the fact that the excess free OA in the Cs-OA precursor immediately and fully shifts the $PbBr_2/PbBr_3^-$ equilibrium to the $PbBr_3^-$ side, making it fully available for the nucleation. Thus, there exists no inherent mechanism for retaining some precursor for the growth stage. This is analogous to the conventional $CsPbBr_3$ nanocrystal synthesis (*25*), wherein there exists no temporal separation of the nucleation and growth, and the nanocrystal size is usually controlled by the synthesis temperature.

https://www.science.org/doi/10.1126/science.abq3616; SCIENCE 8 Sep 2022 Vol 377, Issue 6613 pp. 1406-1412

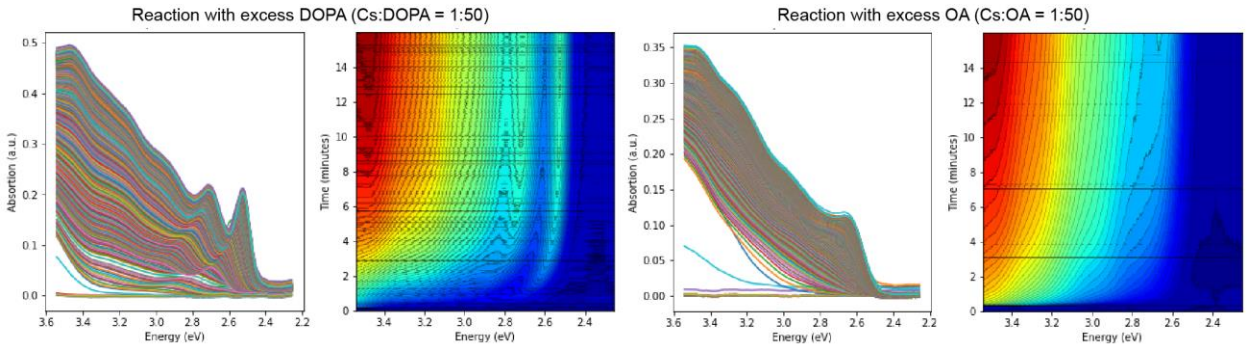

Fig. S12. Comparison of Cs-DOPA vs Cs-OA. Here, the free OA results in the immediate formation of $PbBr_3^-$, vastly accelerating the reaction, as is apparent from the initial increase in OD at the start of the reaction. The fast reaction in this case also leads to the formation of more polydisperse QDs, seen as poorly resolved absorption features.

Modelling of the broadening mechanisms

In the formula $(S5)$ used for calculating the absorption cross-section, the line shape g_{eh} was assumed to have the Voigt profile

$$g_{eh}(x) = V(x,\sigma,\Gamma) = \int_{-\infty}^{\infty} G(x',\sigma)\, L(x-x',\Gamma)\, dx' , \qquad (S20)$$

which is a convolution between the normalized Gaussian $G(x,\sigma) = \frac{1}{\sqrt{2\pi}\,\sigma}\exp(-\frac{x^2}{2\sigma^2})$ and Lorentzian $L(x,\Gamma) = \frac{1}{\pi}\frac{\Gamma}{x^2+\Gamma^2}$ distributions. The total width of the above Voigt function can be approximated with an error less than 0.02% as

$$\mathrm{f}_V = \frac{C_1}{2}\,\mathrm{f}_{\Gamma} + \sqrt{\left(\frac{C_2}{2}\right)^2 \mathrm{f}_{\Gamma}^2 + \mathrm{f}_{\sigma}^2} , \qquad (S21)$$

where $C_1 = 1 + 0.099\ln(2)$ and $C_2 = (1 - 0.099\ln(2))^2$ (*52*). Here, f_σ is the full-width at half-maximum (FWHM) of the Gaussian such that $\mathrm{f}_\sigma = 2\sqrt{2\ln(2)}\,\sigma$ and the standard deviation σ was approximated from the standard deviation of the size variation $\delta_{size} = \delta L/\langle L\rangle$ by using the following Taylor series expansion.

$$\sigma = \sum_i \sigma^{(i)}\,(\delta_{size})^i , \qquad (S22)$$

where $\sigma^{(i)} = (-1)^i\,[(i+1)E_{\mathrm{conf}} + E_{\mathrm{Coul}}]$, E_{conf} and E_{Coul} are the confined kinetic energy and Coulomb interaction energy, respectively. Note that, roughly speaking, $E_{\mathrm{conf}} \propto L^{-2}$ whereas $E_{\mathrm{Coul}} \propto L^{-1}$ and $\sigma^{(i)}$ comes from the derivative of the exciton energy $E = E_{\mathrm{gap}} + E_{\mathrm{conf}} + E_{\mathrm{Coul}}$ with respect to L. Summing up to the fifth order derivative shows sufficient convergence of the Taylor expansion. The Gaussian distribution of width σ represents the static inhomogeneous broadening due to the random distribution of the QD sizes, which is practically independent of temperature T.

https://www.science.org/doi/10.1126/science.abq3616; SCIENCE 8 Sep 2022 Vol 377, Issue 6613 pp. 1406-1412

Apart from σ, there is also some T-dependent contribution to the line width that, in our current work, was modelled under the assumption that all transitions receive the same amount of homogeneous broadening. The largest contribution to this homogeneous broadening coming from the interaction with longitudinal-optical (LO) phonons was supposed to involve only a single effective phonon mode E_{LO}. Additionally, the T-dependent FWHM f_Γ for the Lorentzian function can be written as

$$\mathrm{f}_\Gamma = 2\Gamma = 2\,(\Gamma_0 + \sigma_{Ac}T + \Gamma_{LO}\,N_{LO}). \qquad (S23)$$

The first term Γ_0 characterizes the amount of residual spectral broadening at $T = 0\ K$. The second expression, which is linear in T, describes the interaction with acoustic phonons. Γ_{LO} is the electron-LO phonon coupling rate assuming the perturbative interaction where the total rate is proportional to the phonon occupation number $N_{LO} = \frac{1}{\exp\left(\frac{E_{LO}}{k_B T}\right)-1}$, which follows the Bose-Einstein statistics.

The measured Γ_0 from single-dot spectroscopy shows $\Gamma_0 = 0.4$ meV for $CsPbBr_3$ (*53*). For our current purpose, we shall let $\Gamma_0 = 0$ without any alteration of the basic conclusions. Taking the experimental values $\sigma_{Ac} = 8{\times}10^{-3}$ meV$/K$ and $E_{LO} = 16$ meV (*53*), we obtained the fitted value of $\Gamma_{LO} = 22$ meV from our experimental data by using nonlinear curve-fitting "*lsqcurvefit*" in GNU Octave. This value of Γ_{LO} from the absorption data is smaller than the value $\Gamma_{LO} = 42$ meV that was deduced from single-dot PL. Most likely, a better description of the homogeneous broadening should also involve multiple LO phonon modes.

Besides the formula $(S23)$ including only one effective LO phonon mode at $E_{LO} = 16$ meV albeit retaining the underlying physical mechanism, we note that the experimental data were better fitted using a pure Gaussian function than a Gaussian-Lorentzian convolution. This observation seems to indicate the fact that the electron-phonon interaction potentially acquires some degree of statistical randomness due to, for instance, the dependence of the phonon spectrum on the QD size L and the distribution of L. The size-dependent estimation of σ based on the size variation δ_{size} reproduces excellently the width of the first absorption peak (at low T) while somewhat overestimate σ for higher transitions. Thus, the mechanism for inhomogeneous broadening may also need to be revisited. As a conclusion, additional experimental and theoretical investigations are required to unveil the fundamental features of the electron-phonon coupling as well as of the broadening mechanism of the absorption peaks.

Splitting among the 1p-1p states

The experimental absorption spectra at 14 K exhibit two distinct peaks for the 1p-1p transitions where the lower-energy peak has twice the integrated area of the one at higher energy. In this Supplementary Note, we base our discussion around the splitting among 1p-1p states on mass and shape anisotropy. We note that the latter has been discussed in Krieg *et al* (*21*). As shown below, while the contributions from these two anisotropic sources are non-negligible, the mass anisotropy may provide an even more significant effect compared to the shape anisotropy.

Ab initio calculations based on the orthorhombic structure result in slightly different masses along the various crystallographic axes (*40, 54*). Among them, the masses along two directions, labelled as $\hat{e}_1$ and $\hat{e}_2$, are very similar (or the same in some calculations) and slightly bigger than the mass m_{33} along the third axis $\hat{e}_3$. We defined the average effective mass $\langle m \rangle$ as follows.

https://www.science.org/doi/10.1126/science.abq3616; SCIENCE 8 Sep 2022 Vol 377, Issue 6613 pp. 1406-1412

$$\frac{1}{m_{11}}+\frac{1}{m_{22}}+\frac{1}{m_{33}}=\frac{1}{\langle m\rangle} \tag{S24}$$

From the expression $(S24)$, the dimensionless mass variations are defined as

$$\left(\frac{\delta m}{m}\right)_{11}=\left(\frac{\delta m}{m}\right)_{22}=-\frac{1}{2}\frac{\delta m}{m},\left(\frac{\delta m}{m}\right)_{33}=\frac{\delta m}{m}, \tag{S25}$$

where the masses along the $\hat{e}_1$ and $\hat{e}_2$ axes have been taken to be equal, i.e. $m_{11}=m_{22}$.

The effect of different masses along the three axes can be treated by considering the corresponding change in kinetic energy as a perturbation, leading to the following Hamiltonian:

$$H_{\delta m}=\begin{pmatrix}\left(\frac{\delta m}{m}\right)_{11}\frac{k_1^2}{\langle m\rangle} & 0 & 0\\ 0 & \left(\frac{\delta m}{m}\right)_{22}\frac{k_2^2}{\langle m\rangle} & 0\\ 0 & 0 & \left(\frac{\delta m}{m}\right)_{33}\frac{k_3^2}{\langle m\rangle}\end{pmatrix}. \tag{S26}$$

Note that $\frac{k_i^2}{\langle m\rangle}$ in Eq. $(S26)$ gives the kinetic energy of the 1p state along direction $\hat{e}_i$ when applied on the corresponding wave function. This renders the calculations of 1p-1p splitting due to the mass variation semi-analytical. We chose to work in the EMA with cubic confining potential to also incorporate the anisotropic shape that is described by the aspect ratio below.

$$b_x=b_y=b>1 \tag{S27}$$

The condition in $(S27)$ is equivalent to L_x and L_y being equal to each other and bigger than L_z, which implies that the p_z state with quantum number $(n_x,n_y,n_z)=(1,1,2)$ is higher in energy compared to the $p_{x/y}$ state with $(n_x,n_y,n_z)=(2,1,1)$.

Let $\Delta E_{\mathrm{1p}}^{\delta m/m}$ and $\Delta E_{\mathrm{1p}}^{b}$ be the amount of splitting coming from the mass and shape anisotropy respectively. Briefly speaking, $\Delta E_{\mathrm{1p}}^{\delta m/m}$ is the difference in the energies of the wave functions along $\hat{e}_{1/2}$ and $\hat{e}_3$ whereas $\Delta E_{\mathrm{1p}}^{b}=E_{\mathrm{conf}}^{\mathrm{cube}}(1,1,2)-E_{\mathrm{conf}}^{\mathrm{cube}}(2,1,1)$ is the difference in the confined kinetic energies along L_x and L_z. The upper and lower bounds for the 1p-1p splitting can be obtained by looking at the relative orientation between the crystallographic axes and the edges of a QD. When $\hat{e}_3$ is aligned along L_z, the total splitting amongst the 1p-1p transitions is

$$\Delta E_{\mathrm{1p}}^{\mathrm{U}}=\Delta E_{\mathrm{1p}}^{\delta m/m}+\Delta E_{\mathrm{1p}}^{b}. \tag{S28}$$

If instead $\hat{e}_3$ is perpendicular to L_z, the splitting is given as the difference between the two contributions $\Delta E_{\mathrm{1p}}^{\delta m/m}$ and $\Delta E_{\mathrm{1p}}^{b}$, i.e.

https://www.science.org/doi/10.1126/science.abq3616; SCIENCE 8 Sep 2022 Vol 377, Issue 6613 pp. 1406-1412

$$\Delta E_{1p}^{L} = \left|\Delta E_{1p}^{\delta m/m} - \Delta E_{1p}^{b}\right|. \quad (S29)$$

Eq. $(S28)$ provides an upper limit ΔE_{1p}^{U} for the splitting involving anisotropic mass and shape while ΔE_{1p}^{L} in Eq. $(S29)$ marks the associated lower limit. From the results of the current calculations in **fig. S36**, $\Delta E_{1p}^{\delta m/m}$ is larger than ΔE_{1p}^{b}, which indicates the importance of the mass variation along the various crystal axes, an aspect that has not received much consideration in the literature so far. The parameter choice leading to this observation will be discussed next.

Our SAXS measurements suggest an aspect ratio roughly $b = 1.03$. Ab initio calculations by Traoré *et al* (*40*). imply a level of mass variation of about $\delta m/m = 10\%$ from various DFT flavors using the room temperature crystal structure for $CsPbBr_3$. The values of $\Delta E_{1p}^{\delta m/m}, \Delta E_{1p}^{b}, \Delta E_{1p}^{L}$ and ΔE_{1p}^{U} versus the 1s-1s exciton energy $E_{1s\text{-}1s}$ obtained with this choice of $\delta m/m$ and various aspect ratios $b = 1.03, 1{,}05$ and 1.10 are given in **fig. S36**. Here, we note that the measured value of the aspect ratio alone, which describes the p-state splitting due to the QD shape, cannot reproduce the right order of magnitude of the experimental splitting even by using $b = 1.10$, which is certainly exaggerated compared to the measured SAXS data. The proposed mechanism of mass anisotropy with $\delta m/m = 10\%$, however, is able to bring ΔE_{1p} to a good agreement with the measured data even with much smaller shape anisotropy $b = 1.03$, especially considered within the experimental uncertainty from low-T absorption and PLE experiments. Additional calculations with other values of the mass variation $\delta m/m$ (while keeping $b = 1.03$) can be found in **fig. S37**. These results suggest that the p-state splitting is intrinsic, which may come from various anisotropic origins, other than being extrinsic due to the shape of the QDs. In what follows, we speculate potential sources of anisotropy in these perovskite QDs.

Numerous experiments via XRD techniques shows that, for temperature less than 300 K, $CsPbBr_3$ in orthorhombic phase has two roughly equal lattice parameters that are different from the third, to which the theoretical approach conforms (*39, 55, 56*). As the temperature keeps rising beyond 300 K, the crystal structure makes a transition from orthorhombic to the more symmetric tetragonal and, subsequently, cubic phases (*39, 55, 57*). The crystal structure and, as a consequence, the effective mass tensor become increasingly more isotropic, indicating more splitting at low temperature. Together with the broadened line shape at higher T, this conforms with the appearance of a single, well-defined 1p-1p peak at room- T spectra while observing some splitting at low temperature. Some supporting calculations are shown in **fig. S38**.

Recent studies imply that the transition temperature from orthorhombic to tetragonal and then cubic phases may be lowered in QDs of smaller sizes (*58*). Besides, as the size decreases, the degree of lattice distortion and lead-halide octahedral tilting may also be affected. Small perovskite QDs of 5-10 nanometers have been shown to exhibit some cubic structure even at room temperature (*59*). These experiments signify an observable dependence of the crystal lattice and the effective mass on the QDs size. Furthermore, it is worthwhile to mention that certain level of strain can also introduce changes in the effective mass of the nanostructures (*60-62*). This strain-induced variation, which may be ligand-mediated or facet-specific, may possibly depend on the shape being cuboidal or spheroidal.

As a result, and in summary, we put forward the role of mass anisotropy in the splitting of the observed 1p-1p transitions in the optical spectra at low temperatures, which shall be further studied.

https://www.science.org/doi/10.1126/science.abq3616; SCIENCE 8 Sep 2022 Vol 377, Issue 6613 pp. 1406-1412

Supplementary Tables

Table S1. Reactions from the Main Text.

$CsPbBr_3$						
Figure	**Label**	**Amount of hexane (ml)**	**Amount of $PbBr_2$-TOPO stock solution (µl)**	**Amount of Cs/FA/MA stock solution (µl)**	**Amount of additional TOPO stock solution (µl)**	**Final size (nm)**
Fig 1c	-	6	80	40	160	6.2
Fig 1d	-	0-25	80	40	0	3.1-13
Fig 1e	-	6	2000	1000	0	6.2
Fig 1h/i	483 uM	6	320	160	320	8.2
Fig 1h/i	256 uM	6	160	80	160	6.1
Fig 1h/i	132 uM	6	80	40	80	4.4
Fig 1h/i	34 uM	6	40	20	40	3.4
Fig 1j/k	1:20	6	80	40	240	8.7
Fig 1j/k	1:15	6	80	40	160	6.2
Fig 1j/k	1:10	6	80	40	80	4.4
Fig 1j/k	1:5	6	80	40	0	3.5
Fig 1l*	Conventional	0	4000	75	-	6.3
Fig 1l	Dilution control	6	1280	160	160	7.2
Fig 1l	Dilution + TOPO control	6	40	20	160	7.3
Fig 3e	-	6	80	40	80	4.4
Fig 3f	See Figure 3c/d					
Fig 4b	-	6	160	80	320	8.0
$FAPbBr_3$ and $MAPbBr_3$						
Figure	**Label**	**Amount of hexane (ml)**	**Amount of Pb-TOPO stock solution (µl)**	**Amount of CFA/MA stock solution (µl)**	**Amount of additional DOPA stock solution (µl)**	**Final size (nm)**
Fig 5a	-	6	100	100	100	~7
Fig 5b	6.0 nm	6	100	100	100	6.0
Fig 5b	6.8 nm	6	100	150	100	6.8
Fig 5b	8.8 nm	6	150	250	-	8.8
Fig 5b**	11 nm	6	150	250	-	11
Fig 5e**	-	24	200	200	100	~7
Fig 5f**	5.7 nm	400	800	24000	1000	5.7
Fig 5f**	7.0 nm	24	200	200	100	7.0
Fig 5f**	9.0 nm	400	400	24000	400	9.0
Fig 5f**	9.9 nm	150	250	6000	-	9.9
Fig 6a	$CsPbBr_3$	See Figure 1c				6.8
Fig 6a	$FAPbBr_3$	See Figure 5b				7.2
Fig 6a	$MAPbBr_3$	See Figure 5f				7.0

*Performed with 10 times higher DOPA concentration
** performed with cooling solutions on ice bath prior to injection

https://www.science.org/doi/10.1126/science.abq3616; SCIENCE 8 Sep 2022 Vol 377, Issue 6613 pp. 1406-1412

Table S2. Reaction conditions from Supplementary Information.

$CsPbBr_3$						
Figure	**Label**	**Amount of hexane (ml)**	**Amount of $PbBr_2$-TOPO stock solution (µl)**	**Amount of Cs-stock solution (µl)**	**Amount of additional TOPO stock solution (µl)**	**Final size (nm)**
Fig S1	0.5 mM	6	80	40	320	4.4
Fig S1	1 mM	6	160	40	320	5.4
Fig S1	2 mM	6	320	40	320	7.0
Fig S2	1:2	4.2	800	800	-	7.0
Fig S2	1:320	10.4	1600	10	-	4.5
Fig S3	-	3	20	40	20	-
Fig S4	1:5	6	80	40	80	4.4
Fig S4*	1:75	6	80	40	80	4.6
Fig S5	-	5	800	50	-	4.2
Fig S18	See main text Fig. 1k					
Fig S26**	-	3	20	10	20	4.8
Fig S27	See main text Fig. 3f					

* The amount of DOPA in the Cs-DOPA precursor was increased by 15 times
** Performed on conventional absorption spectrometer

Table S3. Reaction conditions for obtaining preparative quantities of QDs

Size	**Amount of hexane (ml)**	**Amount of $PbBr_2$-TOPO stock solution (µl)**	**Amount of Cs- stock solution (µl)**	**Reaction yield (mg)**
6.5	153	48	24	280
7.4	180	30	15	237
7.9	153	48	24	143
9.0	39	24	12	164
10.3	153	48	24	138

https://www.science.org/doi/10.1126/science.abq3616; SCIENCE 8 Sep 2022 Vol 377, Issue 6613 pp. 1406-1412

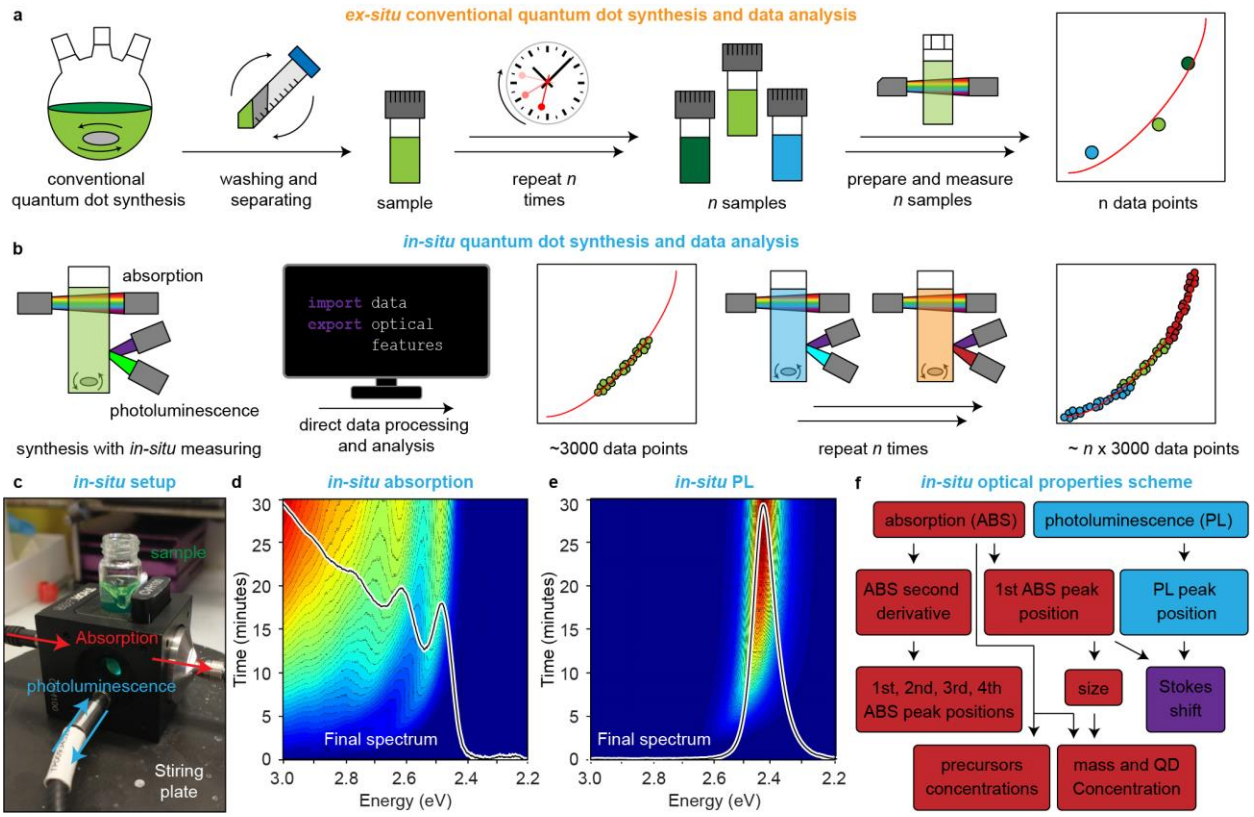

Fig. S13. Comparison between in-situ and ex-situ data analysis and overview of in-situ measurements. A, Schematic showing conventional ex-situ data acquisition and analysis. **B,** Schematic of in-situ acquisition and in-situ analysis. **C,** Setup for in-situ absorption and PL measurements. **D,** Example of in-situ absorption measurement with simultaneous **E,** in-situ PL measurement. **F,** Schematic overview of data analysis of in-situ absorption and PL data.

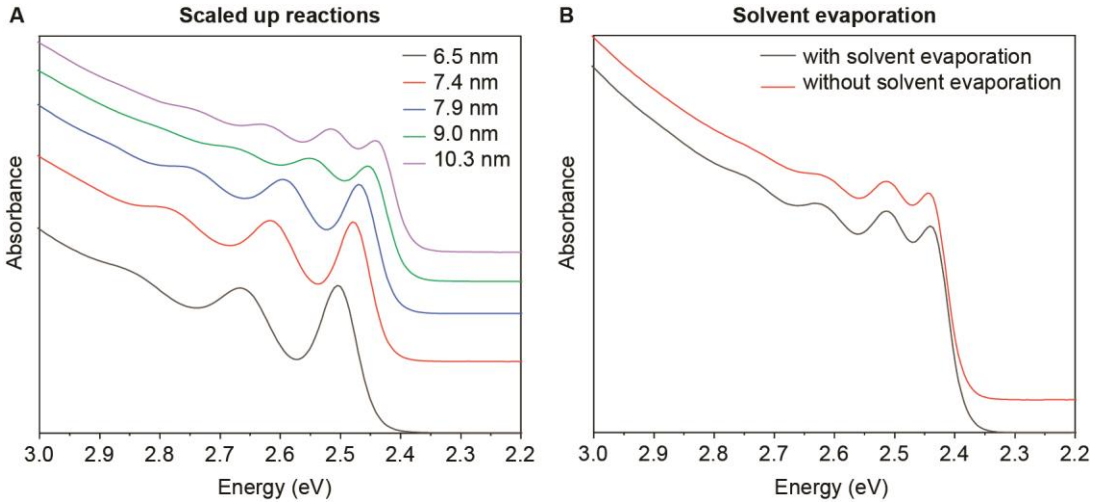

Fig. S14. A, Absorption spectra of $CsPbBr_3$ QDs obtained by scaling the synthesis volume to hundreds mL, yielding hundreds mg of QDs. **B**, Absorption spectra comparing the sample before and after 100-fold concentrating the crude solution of lecithin-capped QDs on rotary-evaporator.

https://www.science.org/doi/10.1126/science.abq3616; SCIENCE 8 Sep 2022 Vol 377, Issue 6613 pp. 1406-1412

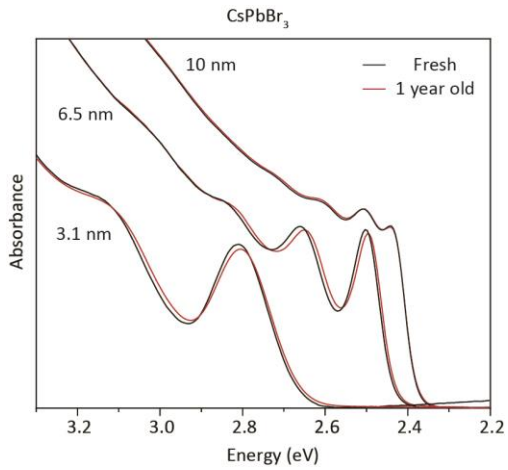

Fig. S15. Absorption spectra comparing as-synthesized $CsPbBr_3$ QDs (as shown in **Fig. 1D**) with the same colloids stored for one year in a glovebox. Note: long-term storage in air often shows signs of slow degradation (aggregation, spectral shifts *etc*.) owing to well-known moisture effects for perovskites.

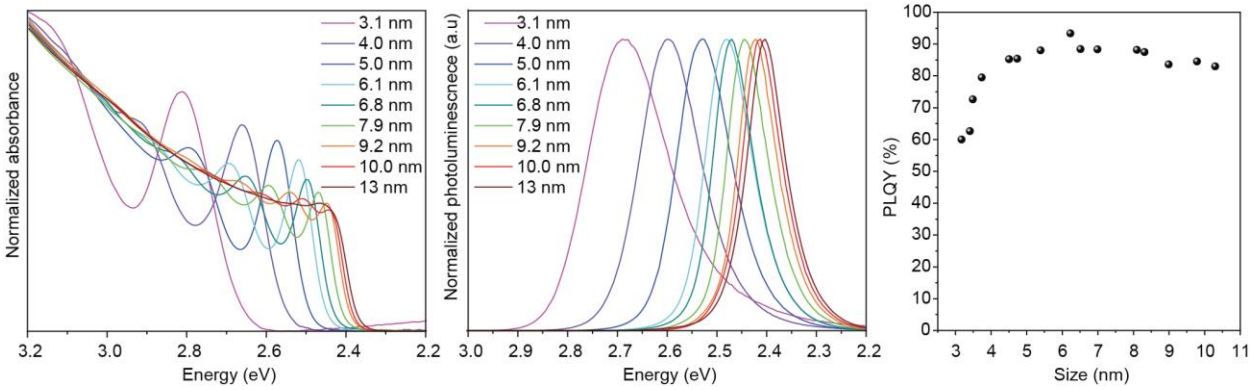

Fig. S16. Additional absorption and PL spectra of purified $CsPbBr_3$ QDs as well as their respective PLQYs.

https://www.science.org/doi/10.1126/science.abq3616; SCIENCE 8 Sep 2022 Vol 377, Issue 6613 pp. 1406-1412

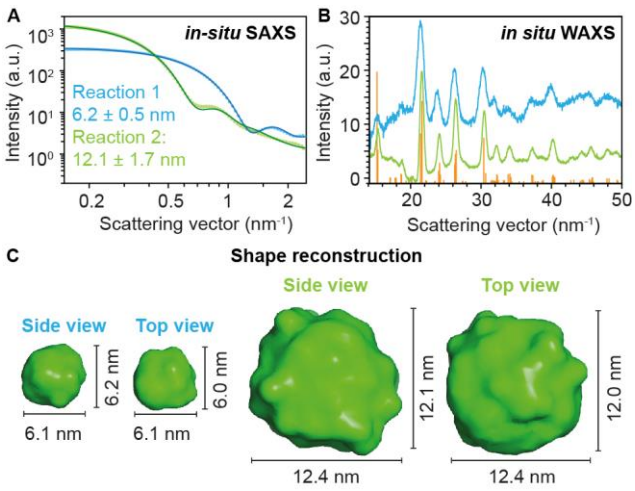

Fig. S17. Additional in-situ SAXS and WAXS measurements of 12 nm $CsPbBr_3$ QDs. A, Comparison of in-situ SAXS scattering curve and its fit for 12 and 6 nm $CsPbBr_3$ QDs. **B,** In-situ WAXS pattern of 12 and 6 nm $CsPbBr_3$ QD, both matching with the orthorhombic $CsPbBr_3$ crystal structure. **C,** Particle shape reconstruction (*46*) of 6 and 12 nm $CsPbBr_3$ QDs, both indicating a near isotropic spherical shape.

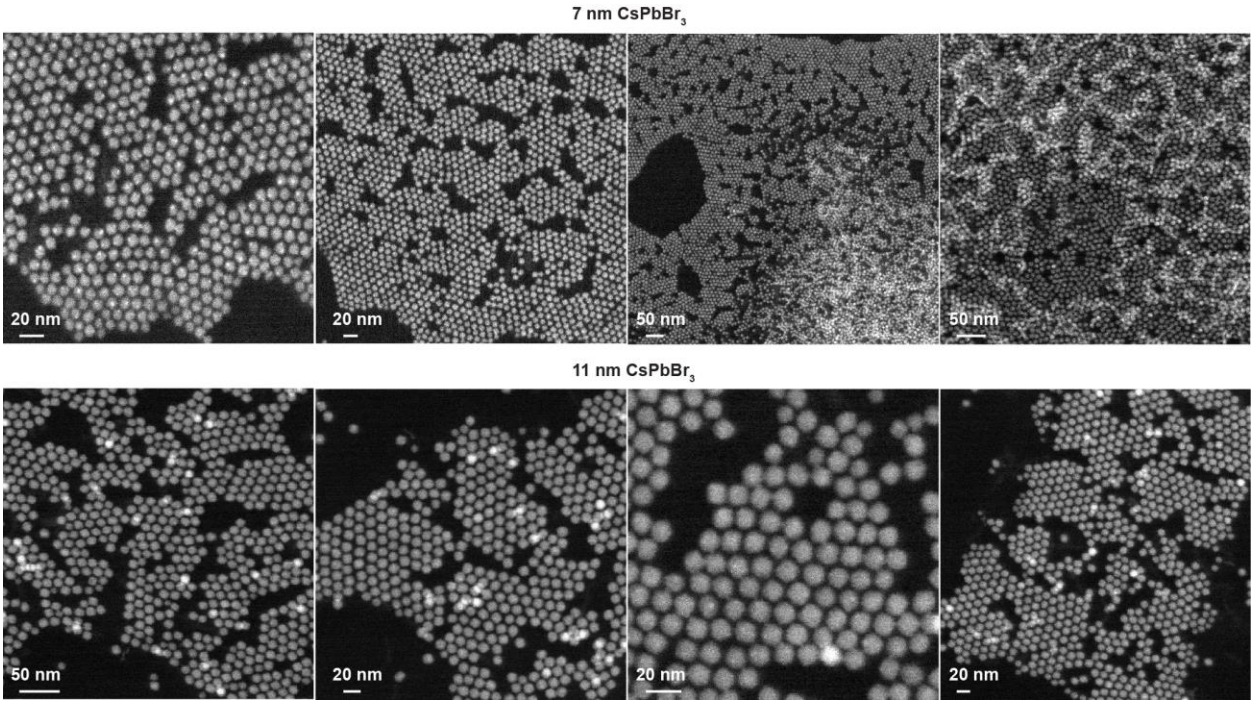

Fig. S18. Additional DF-TEM, HAADF-STEM and HR-HAADF-STEM images of 7 and 11 nm spherical $CsPbBr_3$ QDs. HAADF-STEM images of different sized $CsPbBr_3$ QDs, with larger QDs clearly showing hexagonal assemblies, demonstrating their spheroidal shape.

https://www.science.org/doi/10.1126/science.abq3616; SCIENCE 8 Sep 2022 Vol 377, Issue 6613 pp. 1406-1412

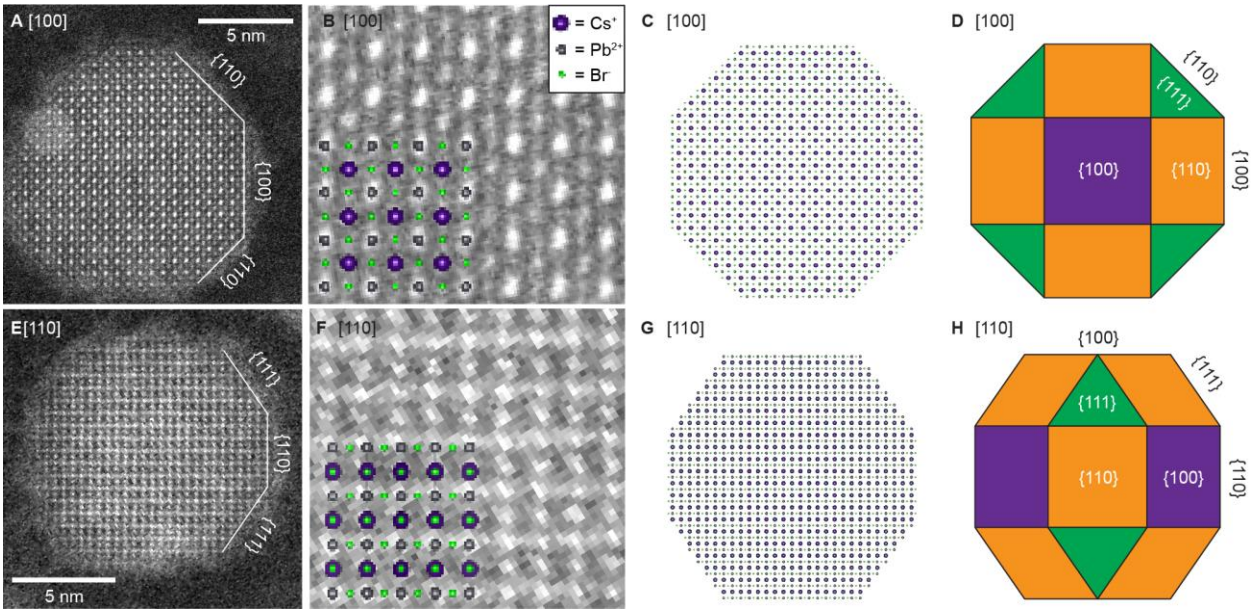

Fig. S19. HR-STEM analysis of 12 nm $CsPbBr_3$ QDs and their rhombicuboctahedral shape. **A,** HR-STEM image of a single 12 nm QD in [100] orientation, showing truncation along {110} facets. **B,** Overlap of HR-STEM image and crystal lattice of $CsPbBr_3$ along [100] axis. **C,** Graphic representation of 20x20x20 unit cell QD truncated along {110} and {111} facets shown along [100] axis. **D,** Simple graphical representation of rhombicuboctahedron shown along [100] axis. **E,** Single QD in [110] orientation, showing truncation along {111} facets. **F,** Overlap of HR-STEM image and crystal lattice of $CsPbBr_3$ along [100] axis. **g,** graphic representation of 20x20x20 unit cell QD truncated along {110} and {111} facets shown along [110] axis. **H,** Graphical representation of rhombicuboctahedron shown along [110] axis.

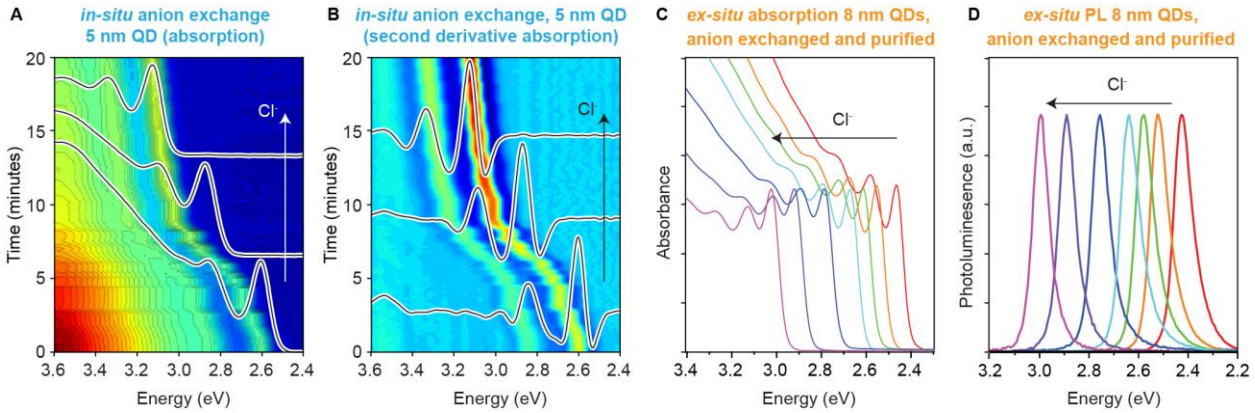

Fig. S20. $CsPbBr_3$ to $CsPbCl_3$ QDs by anion-exchange. A, In-situ recorded absorption spectra of 5 nm $CsPbBr_3$ QDs undergoing controlled Cl^- anion exchange via dropwise addition of Cl^- precursor, with respective second derivative shown in **B. C,** Absorption spectra of a series of purified 8 nm $CsPb(Br:Cl)_3$ QDs with well-resolved higher-order absorption peaks, which remain preserved after the anion-exchange reaction and purification. **D,** Respective PL spectra of QD sample shown in panel **C.**

https://www.science.org/doi/10.1126/science.abq3616; SCIENCE 8 Sep 2022 Vol 377, Issue 6613 pp. 1406-1412

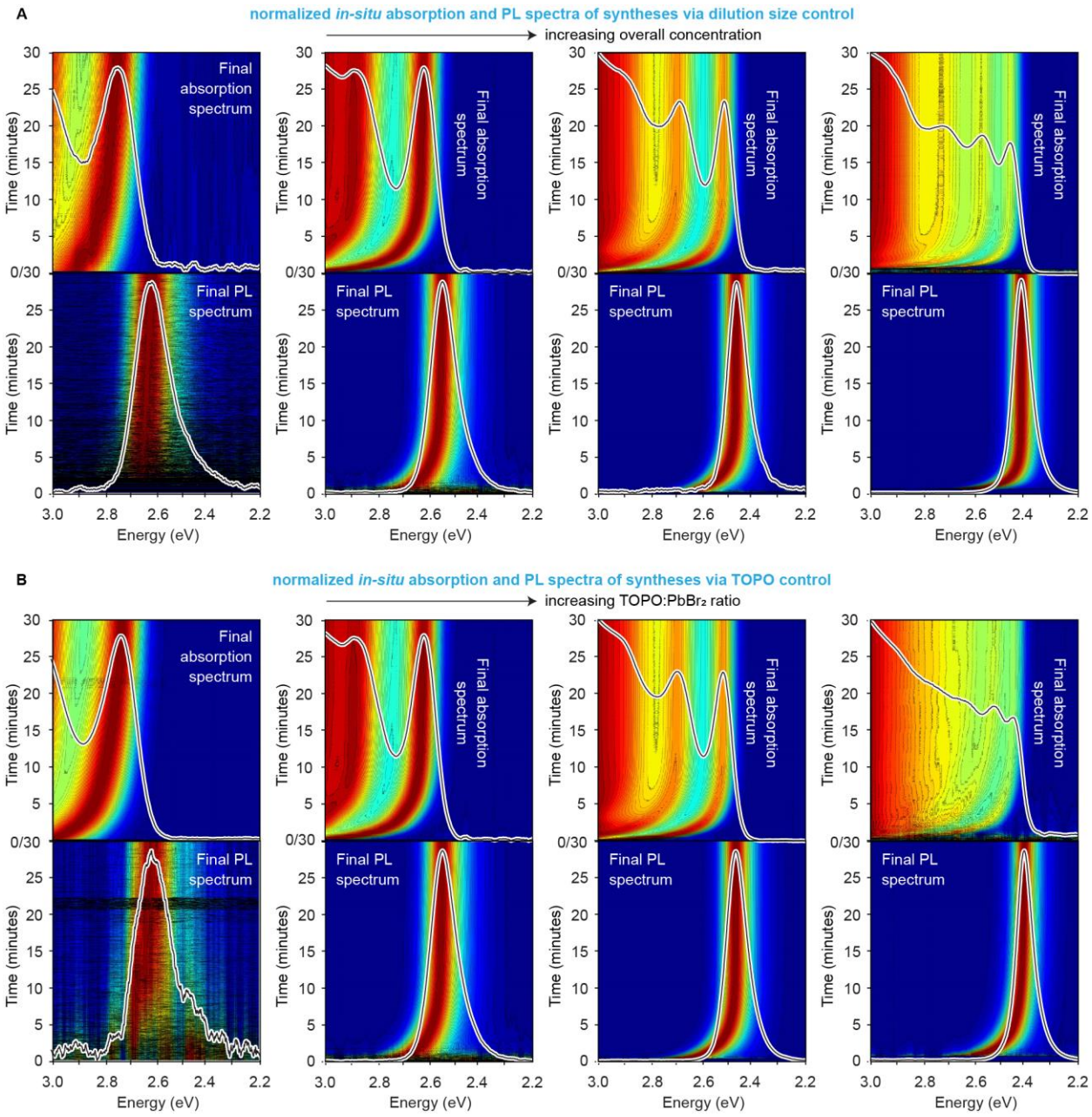

Fig. S21. In-situ measurements of $CsPbBr_3$ QDs synthesized under different growth conditions. A, $CsPbBr_3$ QD size-control by adjusting the overall concentrations. **B,** Size-tuning of $CsPbBr_3$ QDs by increasing the TOPO:$PbBr_2$ ratio. All absorption spectra are normalized at 3 eV for better visual guide of the spectral evolution.

https://www.science.org/doi/10.1126/science.abq3616; SCIENCE 8 Sep 2022 Vol 377, Issue 6613 pp. 1406-1412

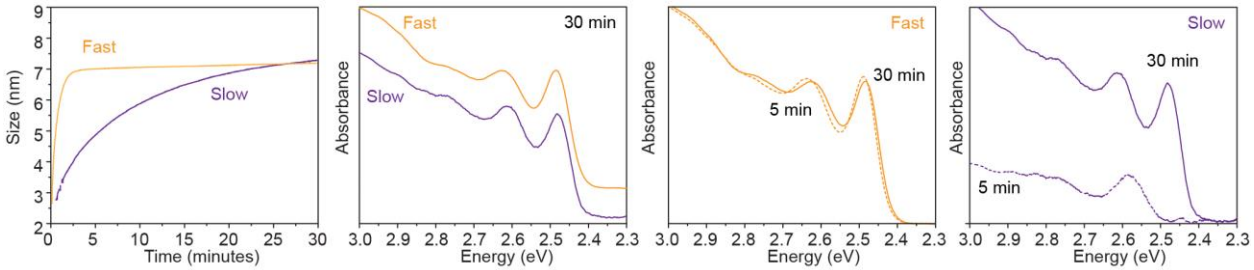

Fig. S22. Different $CsPbBr_3$ QDs obtained using a fast and slow reaction by optimizing the ratio and concentrations of Cs-TOPO, $PbBr_2$ and TOPO.

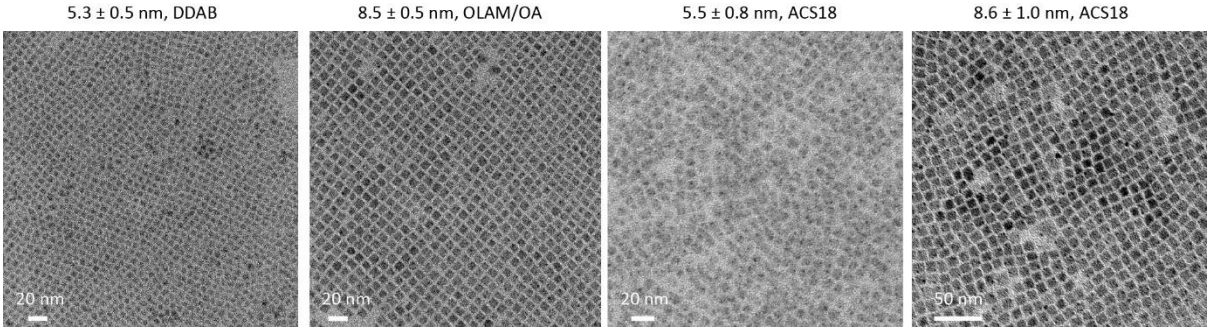

Fig. S23. Size and size-distributions of cuboidal reference $CsPbBr_3$ NCs, synthesized as described in our earlier publications (*20, 21*).

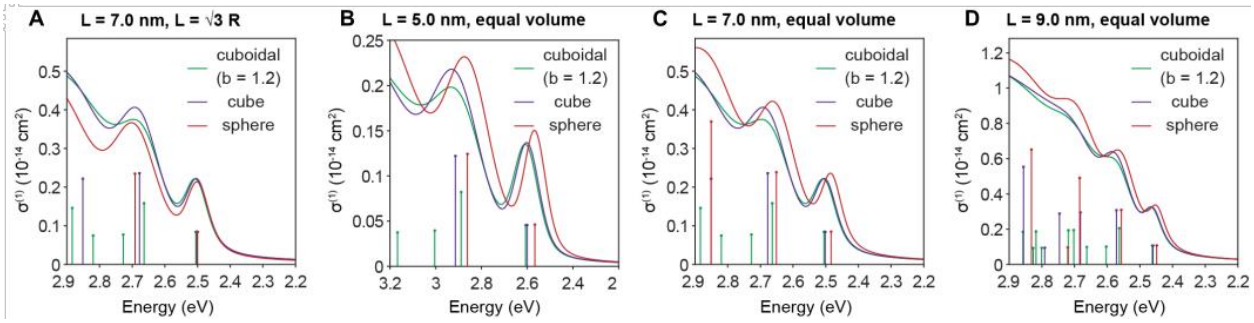

Fig. S24. Additional calculated absorption spectra for comparing cubic and spherical QD shapes. Here, the correspondence between a cube and a sphere was made either using $L = \sqrt{3}\,R$ for $L = 7.0$ nm (panel **A**) or based on matching their volume (panels **B-D**) for three sizes $L =$ 5.0, 7.0, 9.0 nm. The same conclusion as in the main text Figure 2 is reached concerning the absorption spectra of the two geometries: for all sizes computed, the excitonic peaks are better defined for a spherical QD compared to the cubic one, notably for higher order transitions.

https://www.science.org/doi/10.1126/science.abq3616; SCIENCE 8 Sep 2022 Vol 377, Issue 6613 pp. 1406-1412

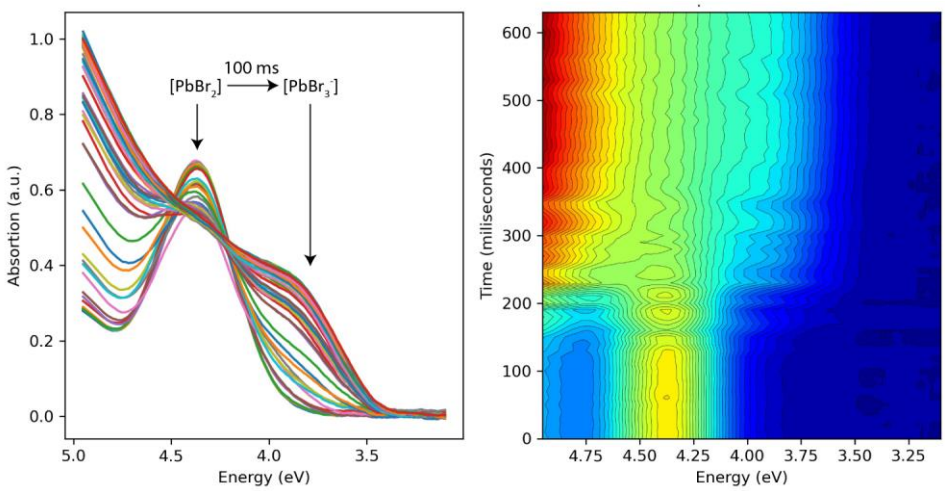

Fig. S25. Millisecond measurement of the formation of $PbBr_3^-$ complex upon the injection of Cs-DOPA into a $PbBr_2$[TOPO] solution.

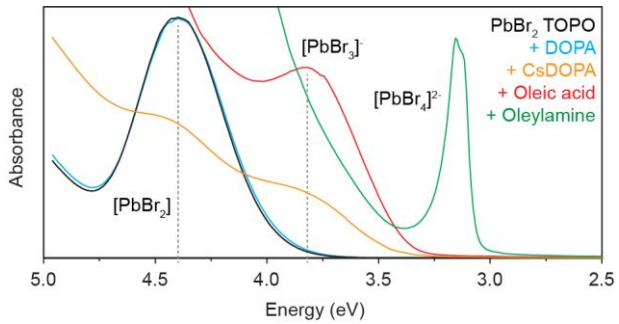

Fig. S26. Reaction of $PbBr_2$[TOPO] with several ligands including DOPA, oleic acid and oleylamine.

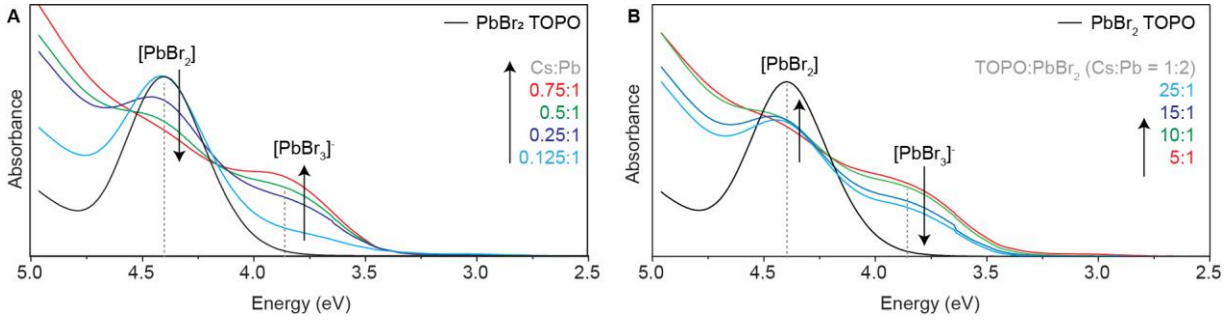

Fig. S27. Absorption spectra of $PbBr_2$ and $CsPbBr_3$ complexes directly after injection of Cs-DOPA with varying Cs:Pb and TOPO:$PbBr_2$ ratios. A, Cs[$PbBr_3$] concentration dependence with varying Cs:$PbBr_2$ ratio (maximum = 0.75). **B,** Cs[$PbBr_3$] concentration dependence with varying TOPO: $PbBr_2$ (minimum = 5).

https://www.science.org/doi/10.1126/science.abq3616; SCIENCE 8 Sep 2022 Vol 377, Issue 6613 pp. 1406-1412

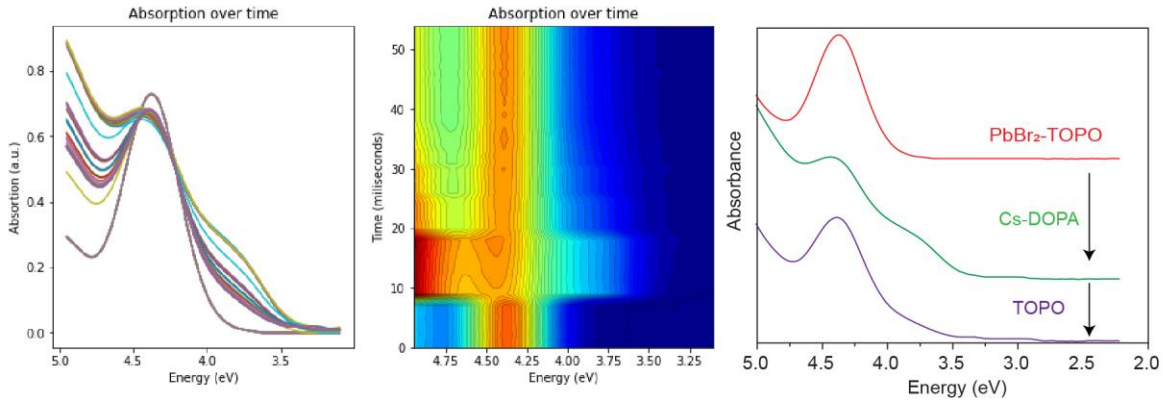

Fig. S28. Demonstration of reversibility of $PbBr_2$:Cs[$PbBr_3$] equilibrium obtained by a fast injection of additional TOPO after the initial Cs-DOPA injection.

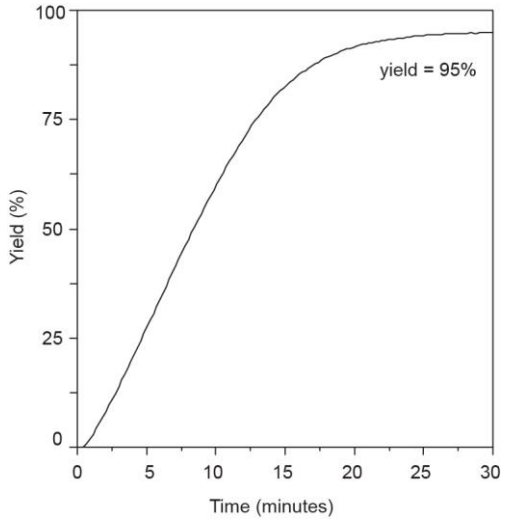

Fig. S29. Example of a typical reaction yield reaching near unity.

https://www.science.org/doi/10.1126/science.abq3616; SCIENCE 8 Sep 2022 Vol 377, Issue 6613 pp. 1406-1412

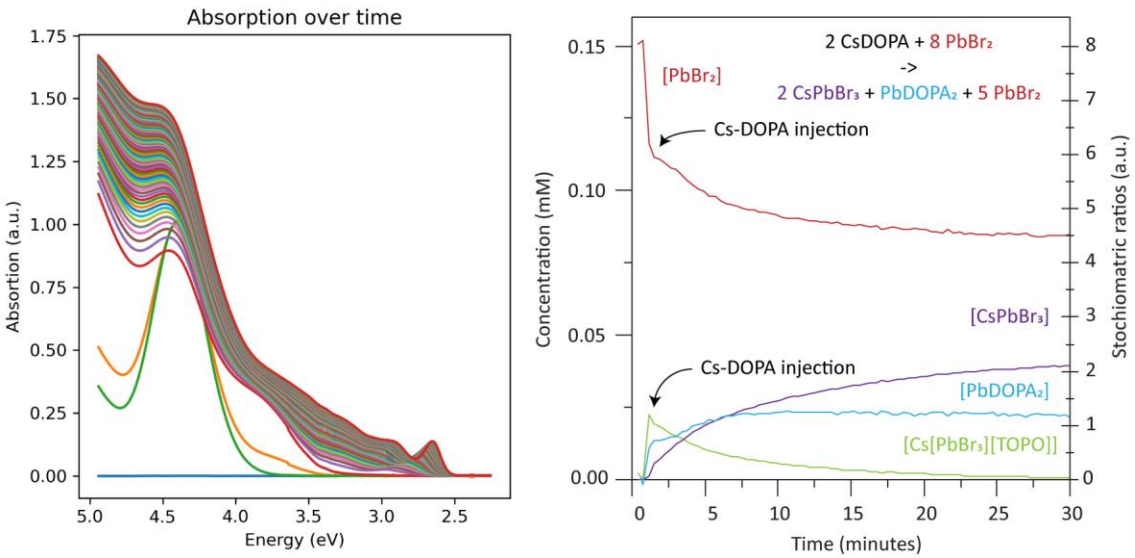

Fig. S30. Absorption spectra and concentration plot of reaction with excess of $PbBr_2$. At the end of the reaction no more $Cs[PbBr_3]$ is present and only 3/8th of the $PbBr_2$ is consumed, confirming that all formed $Cs[PbBr_3]$ is consumed for the formation of $CsPbBr_3$ QDs. These results evidence that the $PbBr_2$:$Cs[PbBr_3]$ equilibrium self-limits the available amount $Cs[PbBr_3]$ for both the initial nucleation, as well as the subsequent growth of $CsPbBr_3$ QDs.

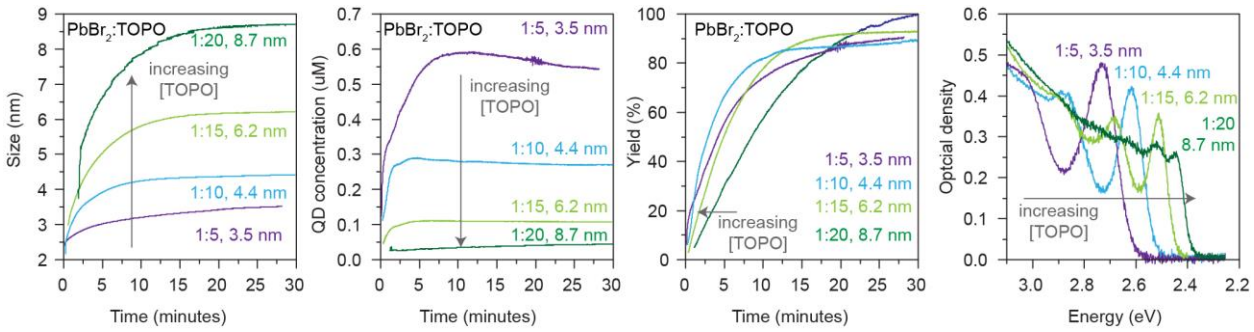

Fig. S31. Further details, including size, QD concentration, reaction yield and final optical absorption spectra of differently sized $CsPbBr_3$ QDs obtained with various concentrations of TOPO.

https://www.science.org/doi/10.1126/science.abq3616; SCIENCE 8 Sep 2022 Vol 377, Issue 6613 pp. 1406-1412

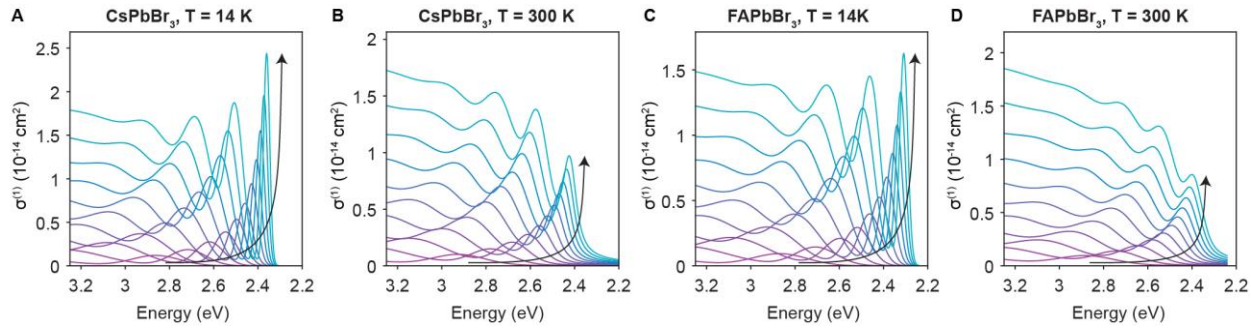

Fig. S32. Theoretical one-photon absorption cross-section $\sigma^{(1)}$ (10^{-14} cm^2) versus energy (eV) for different sizes using spherical k.p model. The direction of increasing size, where $\boldsymbol{L = 3.0 - 8.0}$ **nm** with size step equal to 0.5 nm, is indicated by a black arrow. **A** and **B**, $CsPbBr_3$, **C** and **D**, $FAPbBr_3$. The absorption spectra were calculated at 14 K (panels **A** and **C**) and at 300 K (panels **B** and **D**). The broadening parameters used for $CsPbBr_3$ and $FAPbBr_3$ QDs are discussed in Supplementary Text.

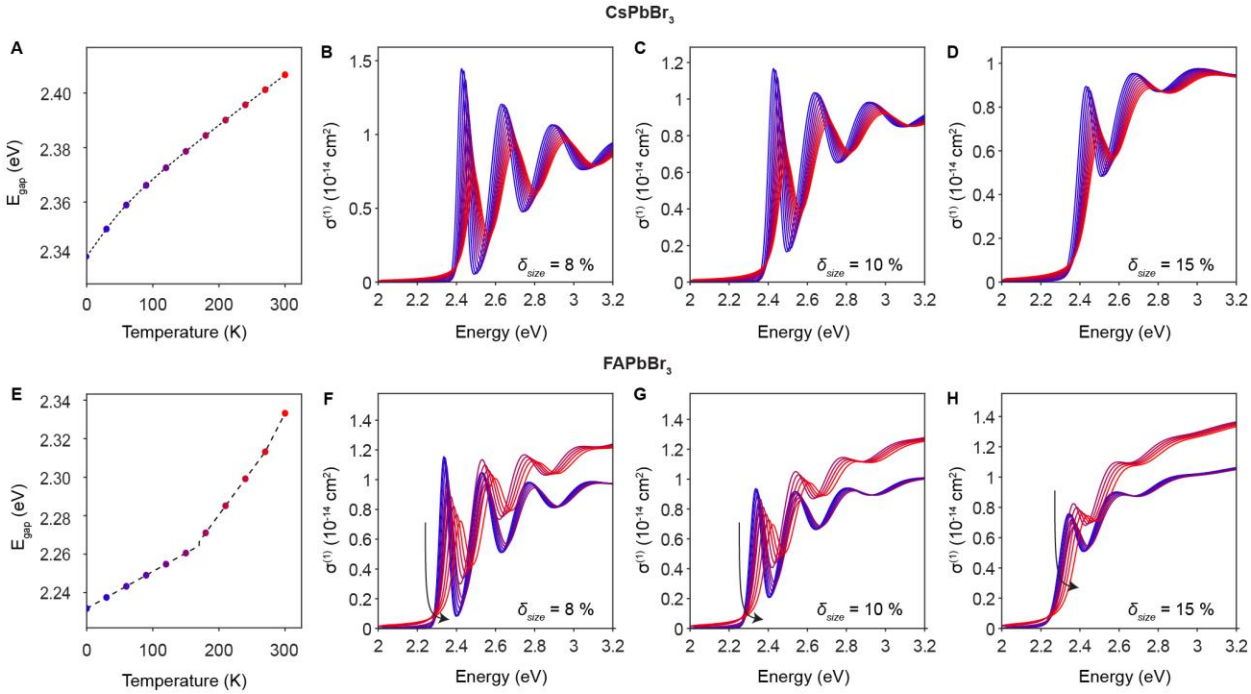

Fig. S33. Temperature dependence of one-photon absorption cross-section spectrum $\sigma^{(1)}$ (10^{-14} cm^2) versus energy (eV) in spherical k.p model. A-D, $CsPbBr_3$, **E-H**, $FAPbBr_3$. QD size is $L = 7.0$ nm for both cations. The arrows denote direction of increasing temperature. Each calculated spectrum corresponds to the temperature represented by each dot on the leftmost panels. The size dispersion δ_{size} is 8%, 10% and 15% from left to right (panels **B** to **D** for $CsPbBr_3$, panels **F** to **H** for $FAPbBr_3$). For $CsPbBr_3$, the temperature-dependent electronic band gap is modelled as in Ref (*63*). Using $A_{\text{linear}} = 0.339$ meV$/K$,(*63*) and $E_{LO} = 16$ meV,(*53*) the choice of $A_{LO} = 30$ meV correctly reproduces the absorption band gap of $CsPbBr_3$ as measured by Yang *et al(50).* The change of E_{gap} of $FAPbBr_3$ versus temperature was fitted using linear function for the data from Wang *et al* (*64*).

https://www.science.org/doi/10.1126/science.abq3616; SCIENCE 8 Sep 2022 Vol 377, Issue 6613 pp. 1406-1412

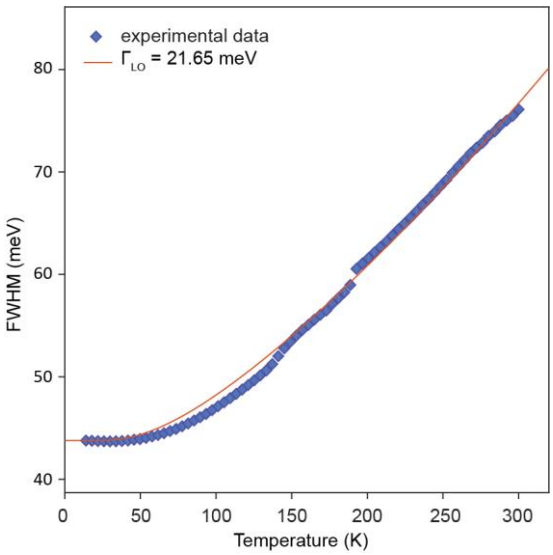

Fig. S34. Full width at half maximum (FWHM) of the lowest-energy absorption transition versus temperature for $L = 7.3$ nm. The experimental data were fitted using Gaussian line shape. Similar fit based on Voigt function closely reproduces the results from Gaussian fit function. The theoretical curve involves Gaussian-Lorentzian convolution to include some temperature-dependent effect. The fitted value $\Gamma_{LO} = 21.65$ meV using electron-phonon coupling with one LO-phonon.

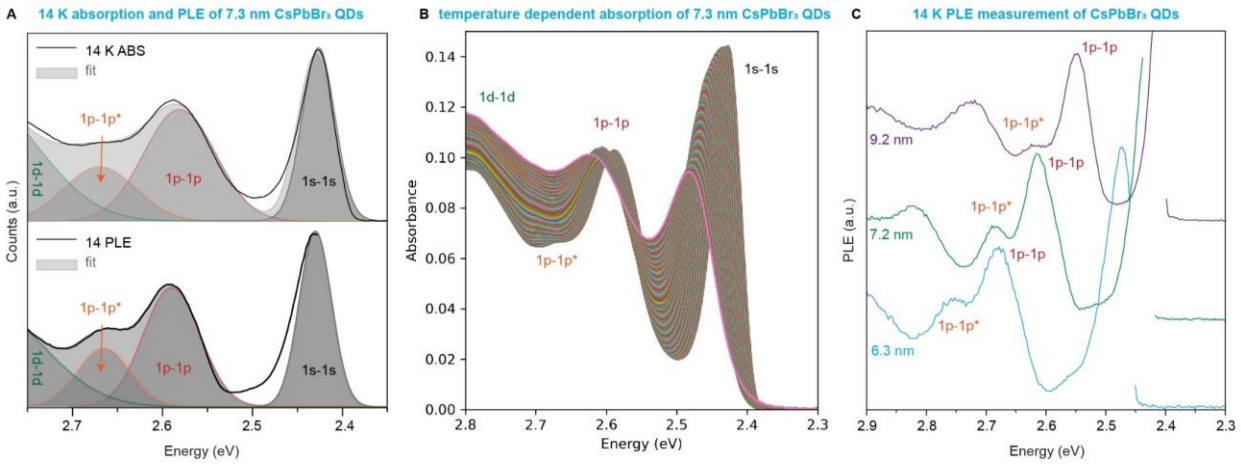

Fig S35. Additional low-temperature absorption and PLE data. A, 14 K absorption and PLE spectra with their respective multigaussian fit, demonstrating splitting of 1p-1p states. The higher-energy 1p-1p has been marked with*. **B,** Temperature-dependent absorption spectra of 7.3 nm $CsPbBr_3$ QD from room temperature to 14 K, showing the appearance of the second high-energy p-p peak around 2.65-2.70 eV. **C,** 14 K PLE measurements of $CsPbBr_3$ QDs in the range of 6-9 nm, all showing a second 1p-1p transition.

https://www.science.org/doi/10.1126/science.abq3616; SCIENCE 8 Sep 2022 Vol 377, Issue 6613 pp. 1406-1412

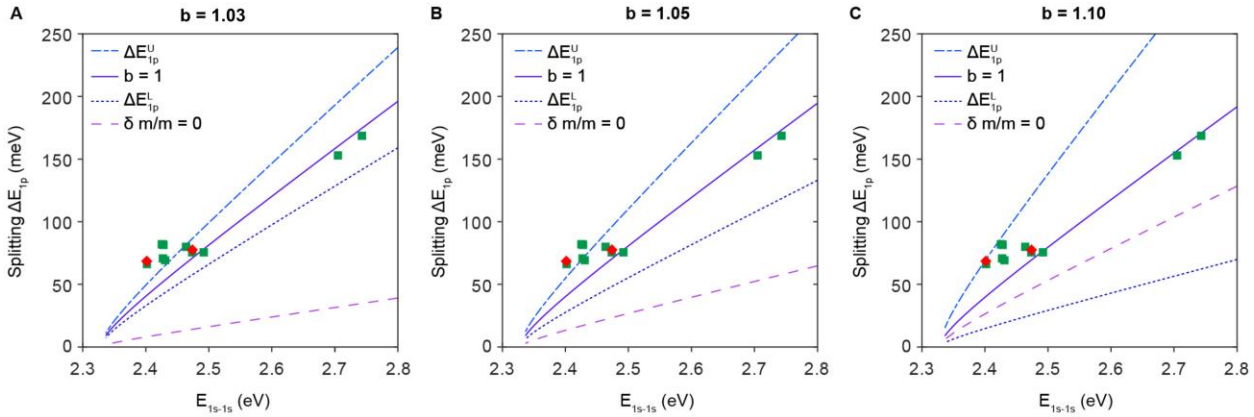

Fig S36. Energy splitting ΔE_{1p} (meV) between the 1p-1p transitions versus the first absorption peak $E_{1s\text{-}1s}$ (eV) for various aspect ratios b. Experimental data points were extracted using second derivative (green square) or multi-Gaussian fit (red diamond) of the absorption spectra. The lines were obtained from theoretical calculations: upper bound ΔE_{1p}^{U} (light blue, dash dotted line), $\Delta E_{1p}^{\delta m/m}$ (solid blue) without shape anisotropy (i.e. $b = 1.00$), lower bound ΔE_{1p}^{L} (dark blue, dotted line) and ΔE_{1p}^{b} (purple dash line) without mass anisotropy (i.e. $\delta m/m = 0$). The dimensionless mass variation was fixed at $\delta m/m = 10\%$ for all three panels. The values of ΔE_{1p}^{b} clearly demonstrate that even using an excessive figure $b = 1.10$ for the extrinsic shape anisotropy, it is impossible to reproduce the measured splitting. This indicates other sources of anisotropy, those that are likely to be intrinsic to materials and syntheses.

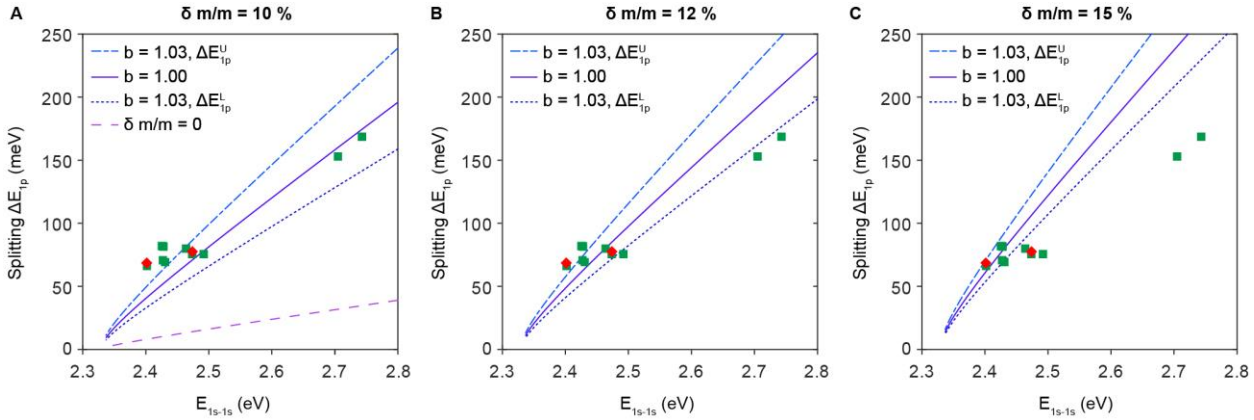

Fig. S37. Energy splitting ΔE_{1p} (meV) between the 1p-1p transitions versus the first absorption peak $E_{1s\text{-}1s}$ (eV) for various mass variation $\delta m/m$. Experimental data points were extracted using second derivative (green square) or multi-Gaussian fit (red diamond) from the low-temperature absorption spectra. The theoretical lines in panels **A-C** were done using the dimensionless mass variation $\delta m/m = 10\%$, 12% and 15%, respectively. Aspect ratio $b = 1.03$. ΔE_{1p}^{U} (light blue, dash dotted line): upper bound; $\Delta E_{1p}^{\delta m/m}$ (solid blue): without shape anisotropy, i.e. $b = 1.00$; ΔE_{1p}^{L} (dark blue, dotted line): lower bound. For panel a, ΔE_{1p}^{b} (purple dash line) was computed without mass anisotropy, i.e. $\delta m/m = 0$, $b = 1.03$, to demonstrate the effect of only shape anisotropy.

https://www.science.org/doi/10.1126/science.abq3616; SCIENCE 8 Sep 2022 Vol 377, Issue 6613 pp. 1406-1412

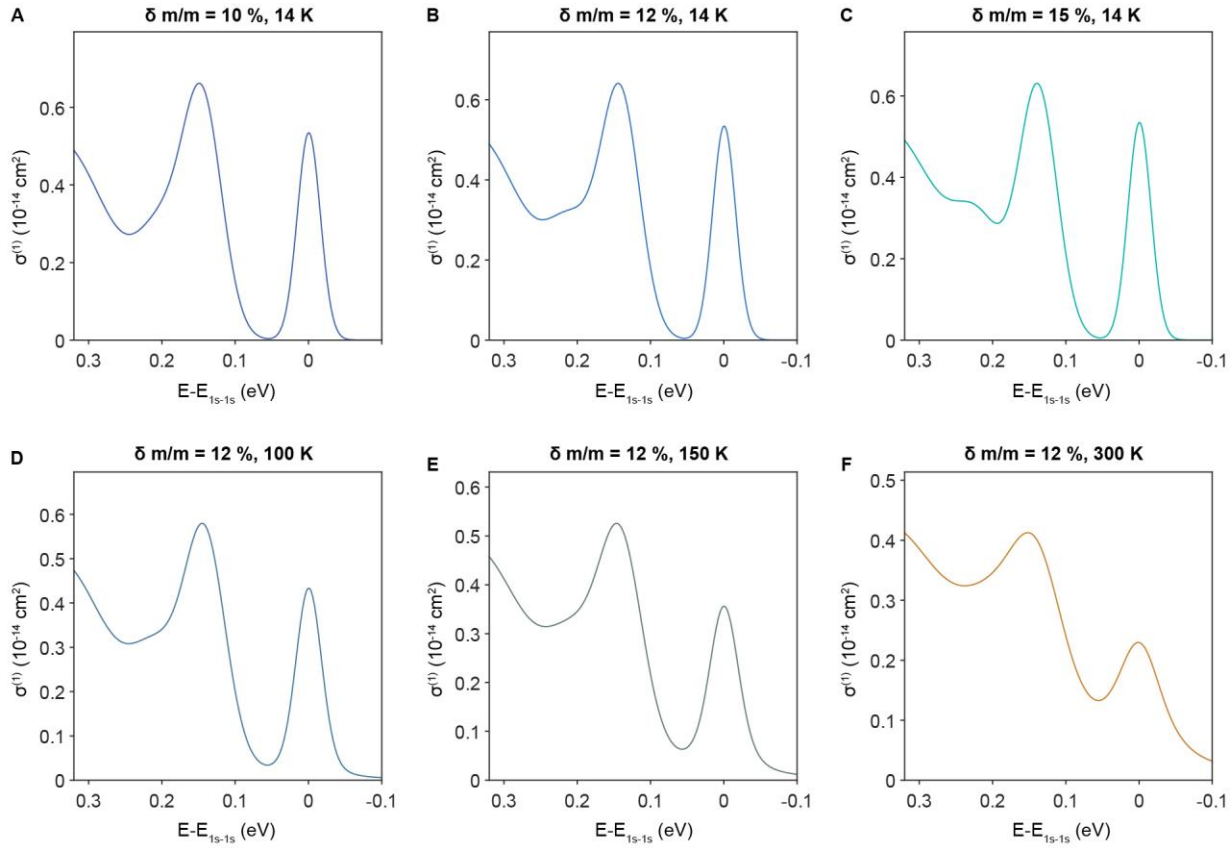

Fig. S38. Theoretical absorption spectra for $CsPbBr_3$ with the splitting in the 1p-1p transition at low temperature. The QD size is $L = 7.3$ nm for which the size dispersion was taken to be $\delta_{size} = 8\%$. The aspect ratio b, as discussed in supplementary text, was fixed 1.03 as obtained from SAXS measurements. The widths of the 1p states were set to be 75% of the estimated line shape outlined in supplementary text for the splitting to be visible. As the mass variation $\delta m/m$ increases from 10% to 12% and then 15%, the separation between the 1p-1p peaks grows bigger as manifested in the spectra in panels a-c at $T = 14$ K. Fixing $\delta m/m = 12\%$, the calculations with increasing temperature where $T = 100$ K, 150 K and 300 K shows that the p-state splitting is no longer observable at room temperature due to thermal broadening.

https://www.science.org/doi/10.1126/science.abq3616; SCIENCE 8 Sep 2022 Vol 377, Issue 6613 pp. 1406-1412

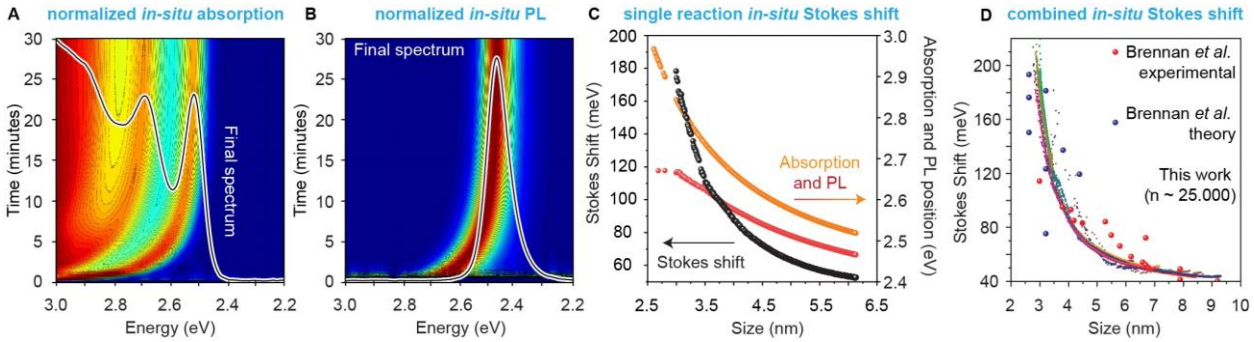

Fig S39. Overview of in-situ Stokes shift measurements. A, Normalized absorption spectra of 6.2 nm $CsPbBr_3$ QD and **B,** corresponding PL spectra. Here, the spectra are normalized at 3 eV to better demonstrate the growth. **C,** In-situ absorption and PL peak positions and the respective calculated Stokes shift as a function of size during the measurement shown in **A-B**. **D,** Size-dependent Stokes shift study of over 25.000 different spectra from 12 different reactions, compared to Brennan *et al (42).*

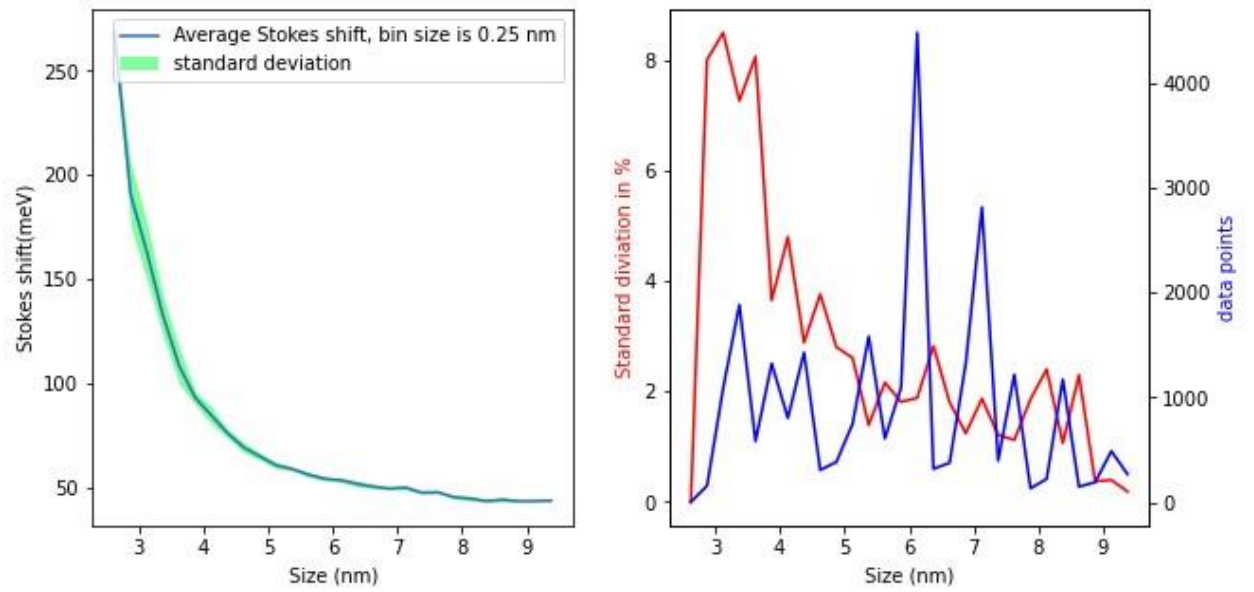

Fig. S40. Average Stokes shift and standard deviation calculation. Here, the Stokes shift data is binned in 0.25 nm parts. Each bin size can then be used to calculate an average Stokes shift for that size with its respective standard deviation.

https://www.science.org/doi/10.1126/science.abq3616; SCIENCE 8 Sep 2022 Vol 377, Issue 6613 pp. 1406-1412

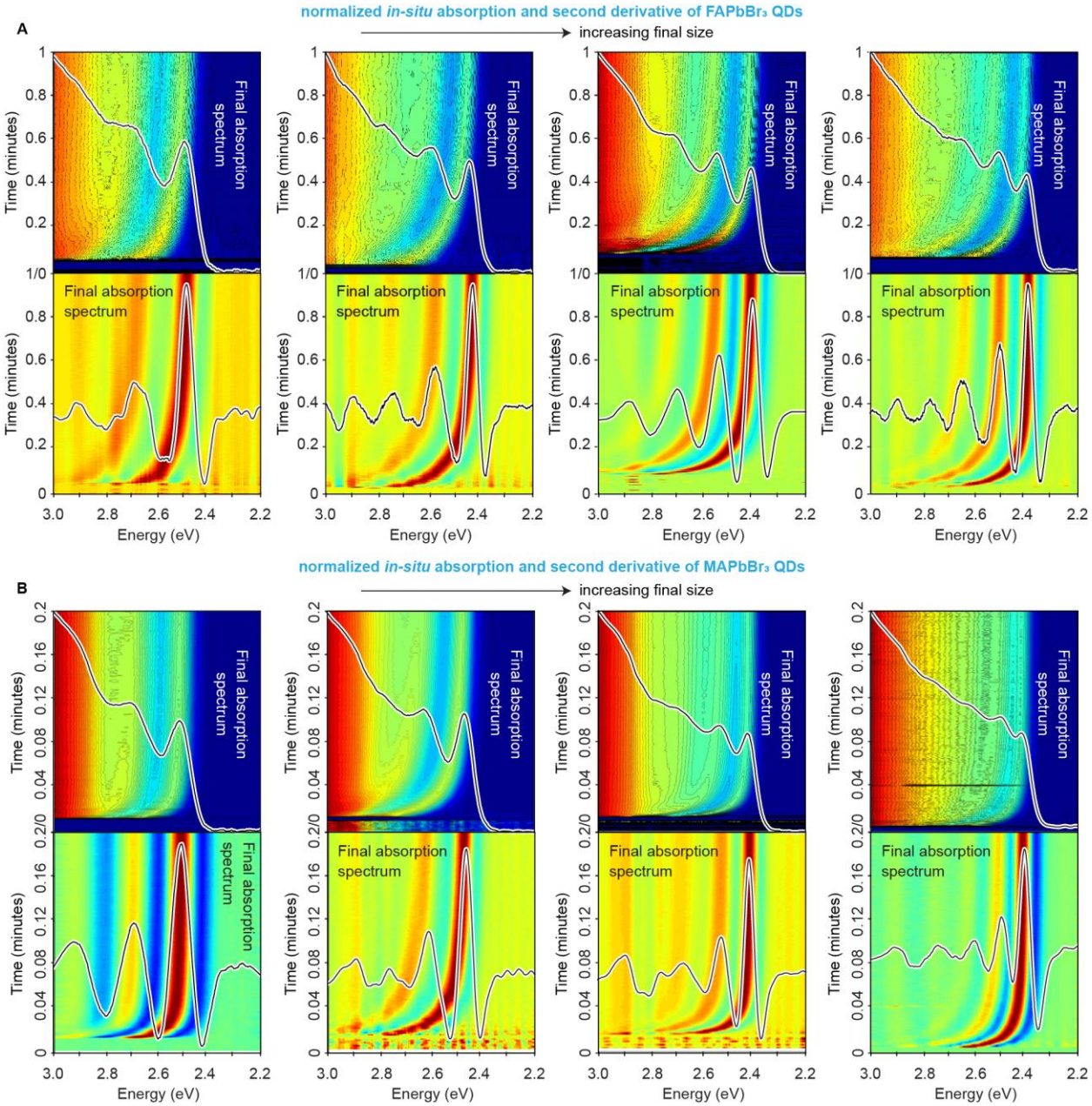

Fig S41. In-situ absorption measurements of $FAPbBr_3$ and $MAPbBr_3$ QDs for different final sizes. The synthesis conditions are found in Tables S1 and S2. **A**, Absorption spectra of $FAPbBr_3$ QDs and their respective negative second derivative, showing the evolution of multiple excitonic absorption transitions. **B**, Analogous study for $MAPBr_3$ QDs. All spectra are normalized at 3 eV for a better visual guide of the spectral changes.

https://www.science.org/doi/10.1126/science.abq3616; SCIENCE 8 Sep 2022 Vol 377, Issue 6613 pp. 1406-1412

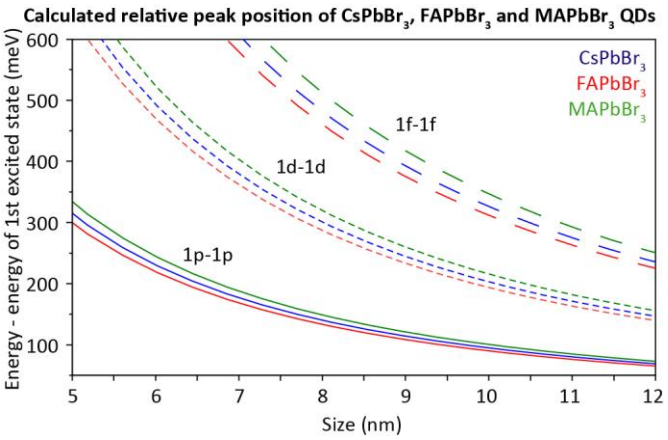

Fig. S42. Calculated relative absorption transition peak position of $CsPbBr_3$, $FAPbBr_3$ and $MAPbBr_3$ QDs as function of QD size, demonstrating relative peak position is independent of the A-site cation.

https://www.science.org/doi/10.1126/science.abq3616; SCIENCE 8 Sep 2022 Vol 377, Issue 6613 pp. 1406-1412

Supplementary Videos

Movie S1. In-situ recorded absorption and photoluminescence spectra during 30-minute growth of roughly 6 nm $CsPbBr_3$ quantum dots.

Movie S2. In-situ recorded absorption of 7 nm $CsPbBr_3$ quantum dots grown at different reaction speeds as reported in Fig 1l.

Movie S3. In-situ recorded absorption of 8.5 nm $CsPbBr_3$ quantum dots with their respective size, quantum dot concentration and mass concentration, extracted from their respective absorption spectra.

Movie S4. In-situ recorded absorption of 8.5 nm $CsPbBr_3$ quantum dots with their respective second derivative, which can be used to extract the position of the first four excitonic absorption transitions.

Movie S5. In-situ recorded absorption and photoluminescence spectra during 30-minute growth of roughly 6 nm $CsPbBr_3$ quantum dots with their respective size depended photoluminescence and first excitonic absorption peak positions. These were used to in-situ determine the size depended Stokes of $CsPbBr_3$ QDs in the range of 3 – 6 nm.

https://www.science.org/doi/10.1126/science.abq3616; SCIENCE 8 Sep 2022 Vol 377, Issue 6613 pp. 1406-1412